International Journal of Impact Engineering 165 (2022) 104229

Contents lists available at ScienceDirect

International Journal of Impact Engineering

journal homepage: www.elsevier.com/locate/ijimpeng

Influence of hybridisation on energy absorption of 3D woven composites under low-velocity impact loading. Modelling and experimental validation

Raúl Muñoz [a,b,*], Rocío Seltzer [c], Federico Sket [a], Carlos González [a,d], Javier Llorca [a,d]

[a] IMDEA Materials Institute, c/Eric Kandel 2, 28906 Getafe, Madrid, Spain
[b] Departamento de Ingeniería Mecánica, Universidad de Salamanca, 37700 Salamanca, Spain
[c] Airbus Defence and Space, Paseo John Lennon s/n, 28040, Madrid, Spain
[d] Department of Materials Science, Polytechnic University of Madrid, 28040 Madrid, Spain

ARTICLE INFO

Keywords:
Textile composites
Impact behaviour
Damage mechanics
Finite Element Analysis (FEA)
X-ray computed tomography

ABSTRACT

This study investigates the low velocity impact behaviour and the energy absorption capability of a hybrid 3D woven composite made from S2-glass (GF), T700 carbon (CF) and Dyneema fibres. The laminate was asymmetric, having a high concentration of CF on one side and GF on the other. Experimental results revealed a pseudo-ductile behaviour of the material and a higher capability to absorb impact energy when glass plies are located at the back face of the laminate. A detailed fractographic analysis by means of X-ray microCT and a FE model was included to explain such differences.

1. Introduction

Unidirectional continuous fibre composites exhibit outstanding in-plane mechanical properties, which makes them particularly suitable for aerospace applications, where high specific strength and stiffness are required. However, composite structures can also be subjected to impact loading by foreign objects during in-service conditions that generate forces in the out-of-plane direction, such as ice shedding, tyre burst, uncontained engine failure in open-rotor designs or tool drop during maintenance operations. Even modest levels of out-of-plane loads generate interlaminar stresses at the interface between layers that may exceed the interlaminar strength of the matrix and cause delamination. The presence of delamination is particularly critical, because it reduces significantly the residual strength in compression of the laminate and is not always visually detectable, as oppose to metals, where impact events typically leave noticeable dents, [1].

To improve delamination resistance of fibre reinforced polymers, which is mainly due to the inherent brittleness of polymer matrices, two main strategies have been reported [2]: improvement of the matrix toughness and modification of fibre architecture. Matrix toughness can be enhanced by adding either toughening particles or nanofibres, or by interleaving polymer films between plies of the laminate [3–6]. Alternatively, fibre architecture can be modified by using 3D textile techniques, such as stitching, z-pinning or 3D weaving.

Stitching significantly suppresses delamination growth [7], particularly in densely stitched composites [8], but it also reduces the in-plane properties of composites due to the damage induced during manufacturing.

Z-pinning technique consists of inserting composite rods orthogonally with respect to the laminate midplane [9]. It delays crack propagation and it is the only 3D reinforcing method that can be applied to prepregs [10], but it significantly reduces the in-plane properties of the laminates [11].

A cost-effective alternative is 3D weaving, particularly the 3D woven orthogonal composites, which according to [12] are the preferred option among 3D composites. The technique consists of manufacturing 3D fabric preforms by interlacing simultaneously three orthogonal sets of yarns: warp, weft (fill) and z-yarn (or z-binder) and then infusing the resin by means of any RTM technique, [13]. The process can be readily automatised in traditional weaving looms with little modification and it enables designers to produce near-net-shape preforms with complex shapes. The manufacturing process is quite flexible, which leads to a large variety of mechanical properties depending on the weave parameters [14], z-yarn inclination [15] and fibre types.

Mechanical testing of 3D woven composites have consistently shown that the through-thickness reinforcement reduces the size of delamination compared to 2D laminates, [16,17]. For instance, [18] tested 2D and 3D woven glass/epoxy composites of the same areal density under

* Corresponding author.
E-mail address: raul.munoz@usal.es (R. Muñoz).

https://doi.org/10.1016/j.ijimpeng.2022.104229
Received 8 July 2021; Received in revised form 22 February 2022; Accepted 21 March 2022
Available online 24 March 2022

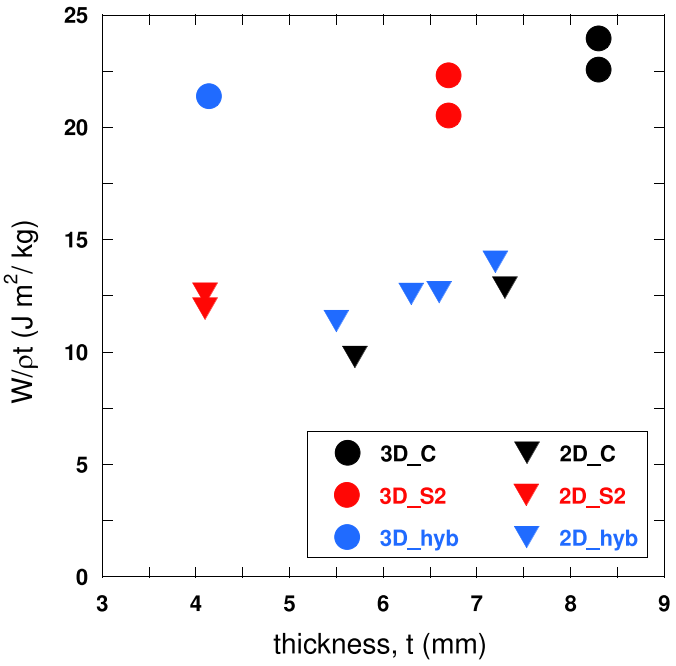

Fig. 1. Energy dissipated during impact, normalized by the areal density ρt, as a function of the laminate thickness, t [21]. Data for 2D laminates with carbon fibres and hybrid S2/C reinforcements were taken from [31].

low-velocity impacts of up to 25 J and concluded that delamination onset occurs at the same load level, but delamination was greater in 2D composites. Likewise, Saleh et al. [19] investigated the low-velocity impact behaviour of four fibre architectures (non-crimp fabric, 2D plain weave, 3D orthogonal and twill) and concluded that damage was the least in 3D woven architectures. Ballistic tests conducted by [20] revealed that delaminated area found in 3D woven targets was significantly smaller than in 2D targets, although no differences were found in terms of ballistic limit. Seltzer et al. [21] compared the impact performance of 2D laminates and 3D woven composites made of different fibre types and concluded that the specific energy absorbed (energy divided by the areal weight) by 3D woven composites was, regardless of the fibre type, twice higher than that of 2D laminate counterparts due to the presence of the through-thickness binders and the multiple failure mechanisms involved (see Fig. 1).

The combination of different fibre types, namely hybridisation, can also improve the mechanical properties of polymer matrix composites, but the type of fibre and the amount of hybridisation must be carefully

Table 1
Characteristics of the preform provided by 3TEX, Inc.

Layer	Orientation	Fibre type	ρ_{fibre} (kg/m^3)	A_{fabric} (kg/m^2)
7	Fill	Glass	2480	0.427
6	Warp	Glass	2480	0.780
5	Fill	Glass	2480	0.854
4	Warp	Glass	2480	0.780
3	Fill	Glass/carbon	2480 / 1780	0.214 / 0.261
2	Warp	Carbon	1780	0.315
1	Fill	Carbon	1780	0.519
z-yarn	Warp	Polyethylene	970	0.075

Table 2
Volume fraction of fibres as a function of fibre type and orientation within the hybrid composite.

Material	warp (%)	fill (%)	total (%)
Glass S2	15.4	14.7	30.1
Carbon AS4C	4.3	10.7	15.0
Polyethylene SK75	1.9	—	1.9
Total fibres	21.6	25.4	47

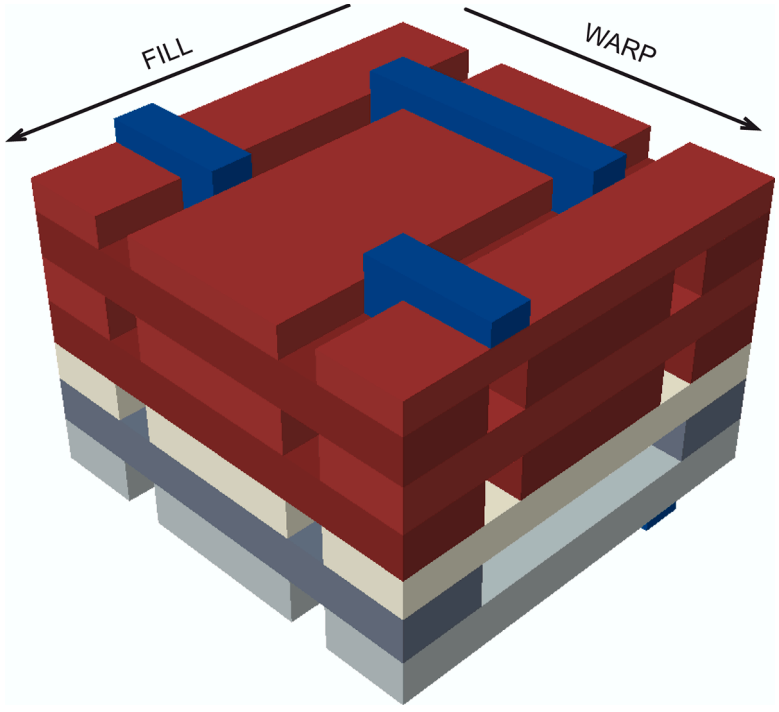

Fig. 2. Schematic of the unit cell of the hybrid 3D woven fibre preform. Carbon fibre bundles are shown in grey (dark grey for the warp direction and light grey for the fill), hybrid bundles in white and glass fibre bundles in red (dark red in the warp direction and light red in the fill direction). PE z-yarn binders in the warp direction are plotted in navy blue. (For interpretation of the references to colour in this figure legend, the reader is referred to the web version of this article.)

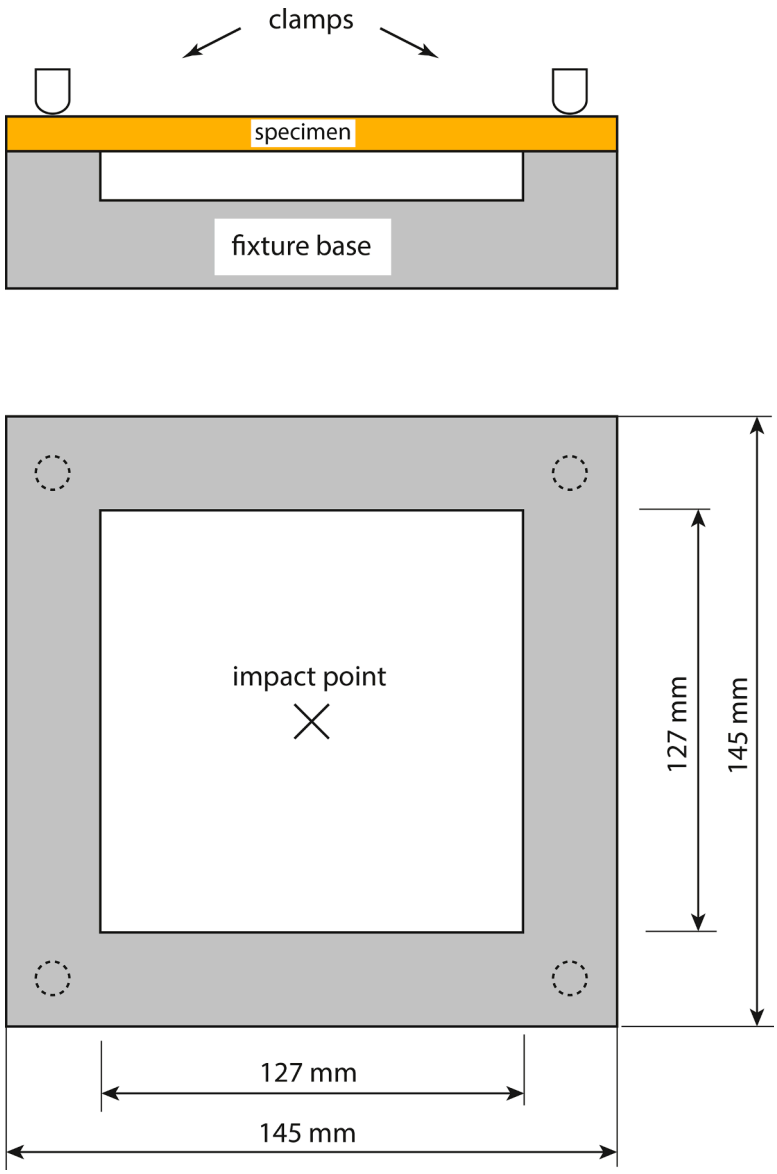

Fig. 3. Schematic drop-weight impact set-up (not-to-scale).

selected, [22–29]. As the outcome of hybridisation cannot be readily predicted with analytical models, numerical models are commonly used, [30].

This work analyses the transversal low velocity impact behaviour of an epoxy matrix composite reinforced with a 3D orthogonal woven fabric made from s2-glass (GF), T700 carbon (CF) and Dyneema fibres (PE). As the 3D woven composite was asymmetric, coupons were impacted alternatively on the carbon fibre (CF) and glass fibre (GF) rich sides to further analyse the influence of hybridisation. The energy absorbed and the failure mechanisms were assessed by using X-ray microtomographic techniques (XCT) and a Finite Element (FE) model.

2. Materials

2.1. 3D Woven composite

A flat composite panel was manufactured by vacuum infusion of an epoxy-vinylester resin (Derakane 8084) into a hybrid 3D orthogonal woven composite. The material was provided by 3TEX, Inc. (Cary, North Carolina, USA) with the commercial name p3w-d00001-hx21. The preform was non-symmetric and consisted of three warp (0) and four fill (90) fibre layers stacked as a cross-ply laminate $[90_c, 0_c, 90_{c/s2}, 0_{s2}, 90_{s2}, 0_{s2}, 90_{s2}]$. The schematic of the 3D fibre preform is shown in Fig. 2. The fibres in each layer were distributed in yarns rectangular in shape. The top four layers were made up of S2 glass fibres and the bottom 2 layers of AS4C carbon fibres. The hybrid layer (containing glass and carbon fibres) oriented in the fill direction was located between the glass and the carbon layers. Each tow of this layer contained both AS4C and S2 glass fibres, which were not intermingled but separated in two different zones of the tow (i.e. one half of the tow was formed by carbon fibres and the other half by glass fibres). In addition, the composite panel was reinforced in the through-thickness direction by z-yarn binders made up of ultra-high molecular weight polyethylene (PE) fibre (Dyneema SK75) that went from top to bottom layers in the warp direction. Note that consecutive z-yarns were in *antiphase*.

The nominal thickness of the composite was 4.1 mm, with an areal density of 6.44 kg/m^2, a porosity of 11.6% and a fibre volume fraction of $V_f = 47\%$. The latter was calculated using Eq. 1, where n is the number of layers, t is the thickness of the composite, ρ_{fibre} is the volumetric mass density of each fibre type and A^i_{fabric} is the areal density of each fabric layer (Table 1). A summary of the volume fraction of each type of fibre in each direction (warp or fill) is presented in Table 2. The PE fibres

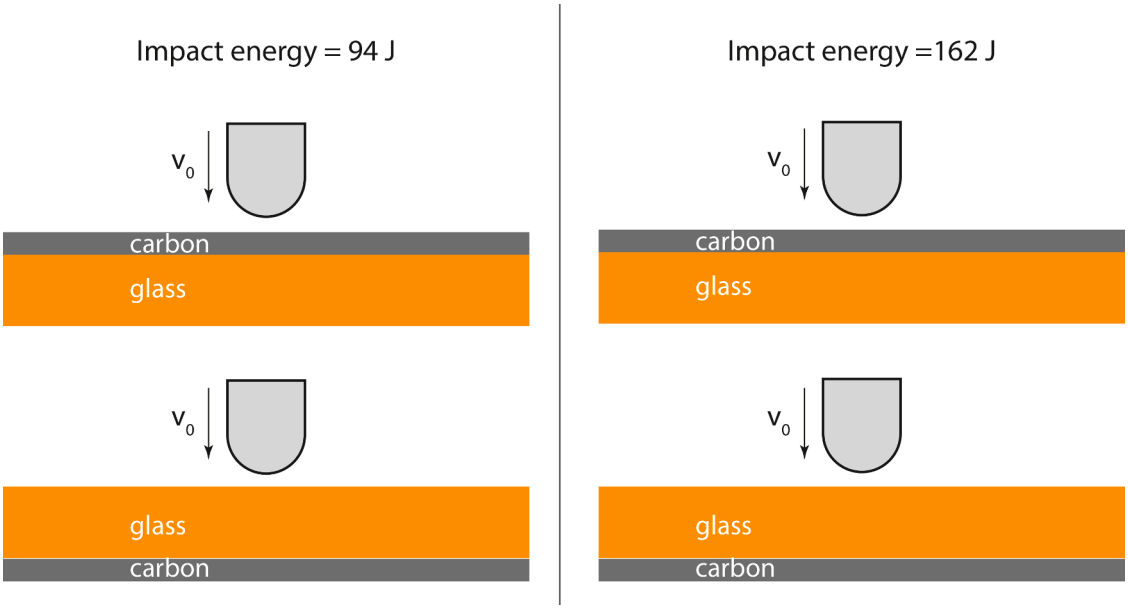

Fig. 4. Schematic of the low velocity load cases: impact of 94 J on carbon and glass faces (left) and impact of 162 J on carbon and glass faces (right).

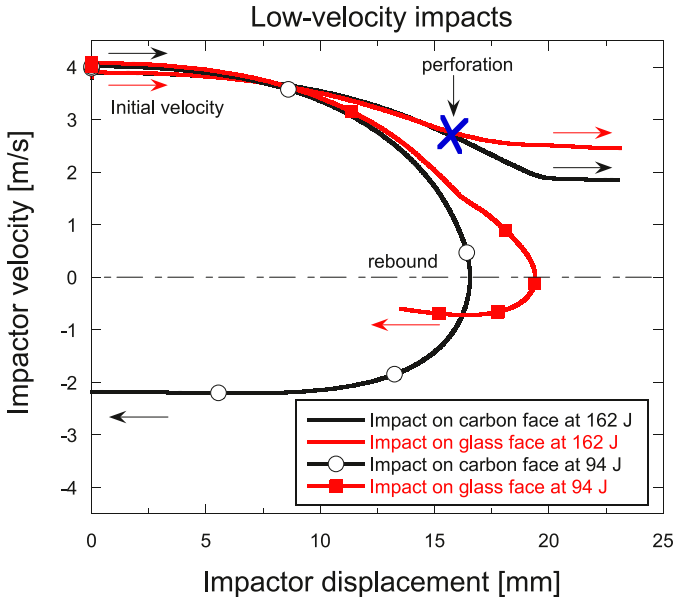

Fig. 5. Velocity of the impactor as a function of impactor displacement. At low energy levels, the impactor rebounds with a residual velocity lower than the initial one when the displacement is close to 15–20 mm. At high impact energies, the impactor is able to perforate the plate and the velocity is always positive.

represent the 1.9% of the volume of the composite.

$$V_f = \sum_{i=1}^{n} \frac{1}{t} \left(\frac{A^i_{\text{fabric}}}{\rho_{\text{fibre}}} \right) \tag{1}$$

3. Experiments

3.1. Specimen preparation and test procedure

The composite panels were machined into 145 × 145 mm^2 square plates and clamped by their corners on a hollow square section of 127 × 127 mm^2, Fig. 3.

Four coupons were impacted with energies of 94 J and 162 J, which correspond to potential threats caused by open rotor engines. The energies were sufficiently high to cause severe damage (94 J) and even perforation (162 J). The nominal impact velocity was set to a constant speed of 4 ± 0.2 m/s to avoid potential strain rate effects. As the ratio between the impact velocity and the through-thickness compressive wave speed is much lower than the strain to failure in the thickness direction, the impact can be classified as low-velocity impact, [32]. Each panel was tested on either the carbon fibre or the glass fibre rich faces (from now on, CF and GF, respectively) at the aforementioned impact energies. The four load cases are summarized in Fig. 4.

The low velocity impact tests were carried out at room temperature

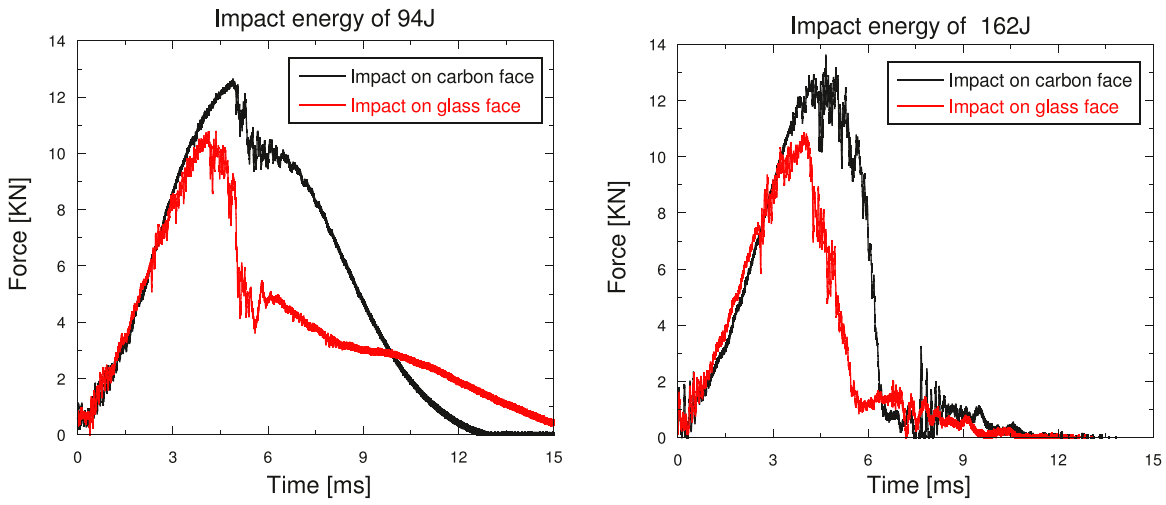

Fig. 6. Force-time curves under low velocity impact (left) without perforation and (right) with perforation.

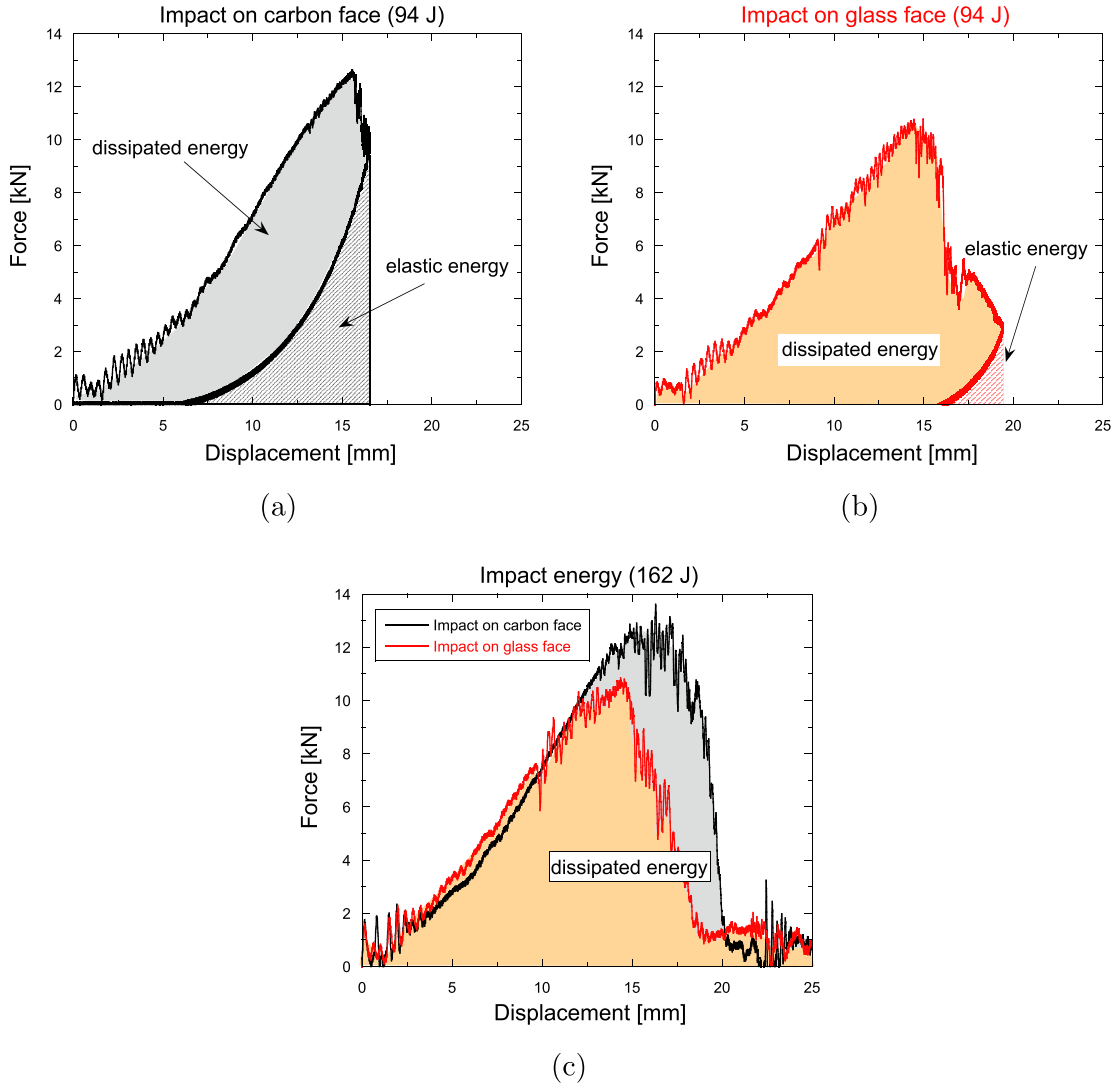

Fig. 7. (a) and (b) Stored elastic energy and dissipated energy at 94 J. (c) dissipated energy at 162 J. Note that the GF configuration was almost perforated, so the amount of elastic energy stored was minimum.

Table 3
Absorbed energy during low velocity impact tests.

	Stored elastic energy (% of 94 J) (no perforation)	Dissipated energy (% of 162 J) (perforation)
carbon face	30	79
glass face	3	65

and humidity using an Instron Dynatup 8250 drop-weight test rig equipped with a pair of rebound catchers to prevent multiple impacts on the tested specimens. The tup was hemispherical with a diameter of 12.7 mm and it was instrumented with an accelerometer. Force and time were recorded in a data acquisition system, from which velocity and displacement can be calculated by integrating the force history according to Eqs. (2) and (3).

$$v(t) = v_i + gt - \int_0^t \frac{F(t)}{M_i} dt \tag{2}$$

$$w_i(t) = \int_0^t v(t)dt = v_i t + \frac{gt^2}{2} - \int_0^t \left(\int_0^t \frac{F(t)}{M_i} dt \right) dt \tag{3}$$

where v_i and w_i are, respectively, the initial velocity and the displacement of the impactor, g the acceleration of the gravity and M_i the mass of the impactor, [33].

Two representative specimens were inspected after failure by X-Ray tomography (XCT), using a Nanotom 160 NF (Phoenix) to obtain detailed information about the actual damage mechanisms through the thickness. A total of 1500 radiographies were acquired during the 360° rotation of the sample with an exposure time of 750 ms. The tomograms resolution was in the range 9–11 μm/voxel, depending on the specimen width.

4. Results

4.1. Impact event

The impact event can be described in terms of the principle of energy conservation. As the impactor comes into contact with the target, a fraction of the initial kinetic energy of the impactor is gradually converted into elastic energy, [34], whereas the remaining energy is dissipated in the form of plate vibrations, friction and fracture.

As shown in Fig. 5, the 94 J impact energy was not sufficiently high to perforate the laminates, i.e., to fracture all layers so that light can pass through [35]. The impactor rebounded with a velocity lower than the initial one due to the energy spent during impact. Interestingly, it was found that the rebound velocity was lower in GF laminates, which suggests that they are more damaged than CF laminates. At 162 J, both laminates were unable to stop the impactor and plate perforation occurred. The residual velocity of the impactor was lower on CF laminates, indicating a higher energy absorption capability than GF laminates.

The force-time histories of the 94 J and the 162 J impacts are depicted in Fig. 6. The response was similar at both energy levels up to the peak load. As the impactor came in contact with the target, some initial oscillations were followed by a gradual increase of the reacting force exerted by the plate. Once fibres started failing, the response became much more unstable and important differences took place between the impact energies considered. At 162 J, fibre breakage occurred in all layers and the force dropped off abruptly as a result of the perforation of the plate, while some fibres did not fail at 94 J, and the impactor was unable to fully penetrate the laminate. The presence of pristine fibres ensured a smoother post-peak response at 94 J, so that the load decreased progressively until the impactor and the plate were no longer in contact. The contact duration was approximately equal to 12–15 ms at low energy levels and 6–7 ms at high energy levels. Further analysis also revealed that hybridisation had a significant influence on the maximum load, which was higher when the impact was carried out on the carbon face.

4.1.1. Energy absorption and damage mechanisms

The quality of a bumper can be determined by its ability to absorb the kinetic energy of the impactor with the minimum damage or, if perforated, by the ability to absorb the maximum amount of energy. While the former can be evaluated by the elastic energy stored, the latter is measured by the energy dissipated, which corresponds to the area under the load-displacement curve.

Fig. 7 shows that coupons impacted on the CF performed better than those impacted on the GF, regardless of the impact energy. CF laminate stored more elastic energy than GF at 94 J, whereas CF laminate dissipated more energy than GF at 162 J. Quantitative results are found in Table 3. Note that in case of perforation, the impactor has a certain residual kinetic energy, which explains why the dissipated energy is not 100%.

The large energy absorption capability of 3D woven composites has already been reported by several authors and is likely due to the presence of the z-yarns [36,37] and the multiple failure mechanisms involved during impact [21,38], which facilitate the dissipation of energy.

The large displacements reached by the impactor (indentation) also revealed that the hybrid 3D composite was very ductile as compared with conventional CFRP laminates. This fact has already been reported in previous investigations under quasi-static tensile [39] and shear tests [40].

XCT inspection of coupons impacted on the glass face at 94 J showed that the deformation of the upper layers of the laminate (glass) was constrained by the presence of the carbon layers at the bottom, which have a lower failure strain. Once the carbon layers failed, the shear plug generated beneath the impactor was pushed outwards, Fig. 8. This mechanism explains the sudden drop observed in the load-displacement curve of the GF 94 J case at a displacement of 17 mm, Fig. 7. In contrast, upper layers are free to deform and the laminate bends smoothly when the ductile layers are located at the bottom (CF configuration), Fig. 9. As the plate bends, the bottom layers of the laminate are subjected to membrane stresses, absorbing a higher amount of energy. This behaviour explains the higher energy absorption capability of the CF configuration.

The impact event was accompanied by multiple failure mechanisms common to both configurations: contact stresses under the impactor caused matrix crushing and shear cracking; yarns were dragged by the impactor, giving rise to tow splitting and also to some tow sliding/debonding at the cross-over sites; z-yarns readily debonded due to the poor adhesion of the polyethylene and, eventually, fibre kinking was also observed in the upper layers as a result of the in-plane compressive stresses developed while bending.

5. Computational model

5.1. Modelling strategy

Three-dimensional composites have a complex geometry, so they are commonly simulated by using unit cells or representative volume elements (RVE) subjected to periodic boundary conditions, [41–43]. This approach requires a time-consuming representation of the geometry and cannot be used in cases where boundary conditions are not periodic, such as transverse loading.

A strategy based on the combination of the embedded element technique and a mesomechanical approach, which can be readily applied to any geometry and boundary condition, has been successfully utilized by the authors to simulate ballistic tests of 3D woven composites, [44]. The mechanical properties of each ply were homogenised and the behaviour was modeled based on continuum damage mechanics. Delamination observed during high-velocity impact tests was taken into

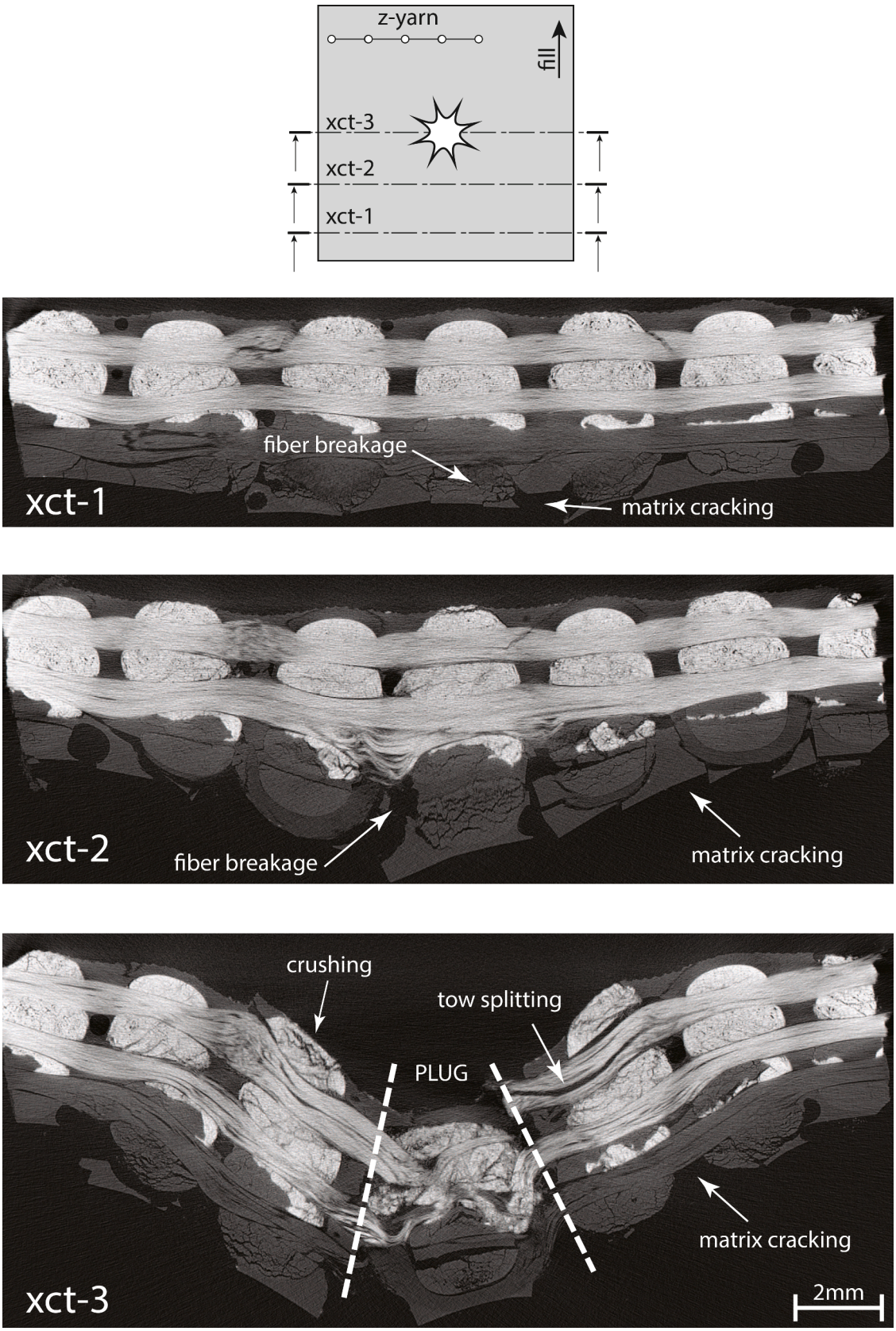

Fig. 8. XCT cross-sections of the imprints left on the 3D hybrid GF configuration after impact at 94 J. The location of each tomogram is specified at the top. GF are in white, while CF, Dyneema and resin are grey. Impact caused large deformations at the centre of the coupon, leading to extensive matrix cracking and fibre breakage at the warp and fill yarns located at the bottom of the laminate. This in turn triggered the formation of a plug which drags warp yarns, causing tow splitting and tow sliding. Crushing was also evident beneath the impactor.

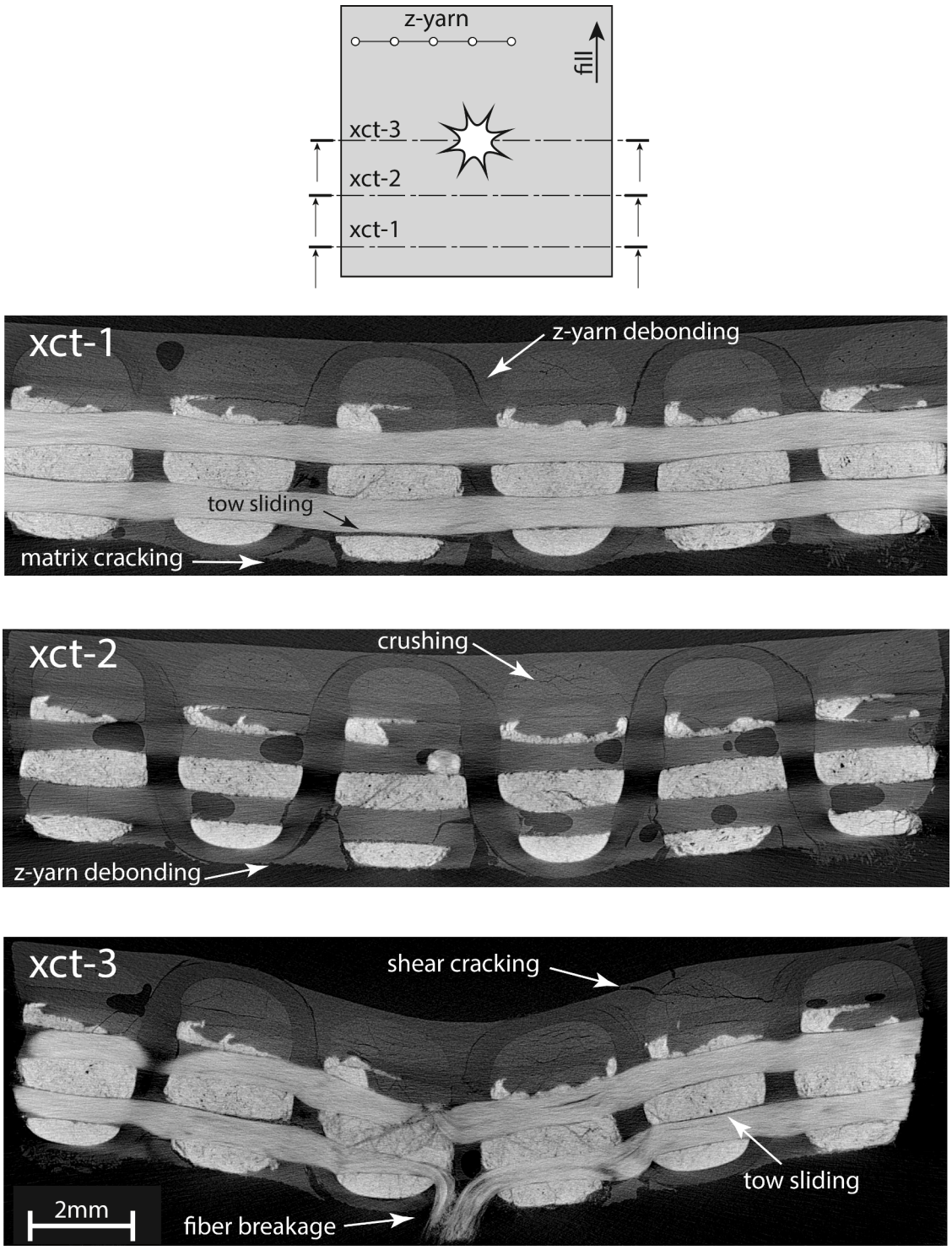

Fig. 9. XCT cross-sections of the imprints left on the 3D hybrid CF configuration after impact at 94 J. The location of each tomogram is specified at the top. GF are in white, while CF, Dyneema and resin are grey. The deformation of the plate was lower and less concentrated than in the GF configuration. Fibre breakage was only evident at the warp yarns located at the bottom of the laminate. There was some shear cracking at the indented face as a result of the brittleness of the carbon fibres.

account with cohesive elements, whilst the through-thickness effect of the PE z-yarns was introduced in the model by means of truss elements embedded into the host finite element mesh. Such modelling strategy was initially applied to simulate the low-velocity impact behaviour of the 3D woven composite studied here. However, simulations showed that once cohesive elements are damaged delamination propagates rapidly, reducing the bending stiffness of the composite. This is not in agreement with experimental observations, where XCT damage inspection revealed that delamination does not occur during low-velocity impact tests, so this modelling approach was eventually discarded. Further details can be found in Appendix A.

An alternative approach is presented below. As plies of the hybrid 3D woven composite are held together during low-velocity impact loading, cohesive elements are not needed. Likewise, z-yarns only contribute to improve delamination resistance, so they can also be removed from the FE model. As a result, this approach correlates better with experimental

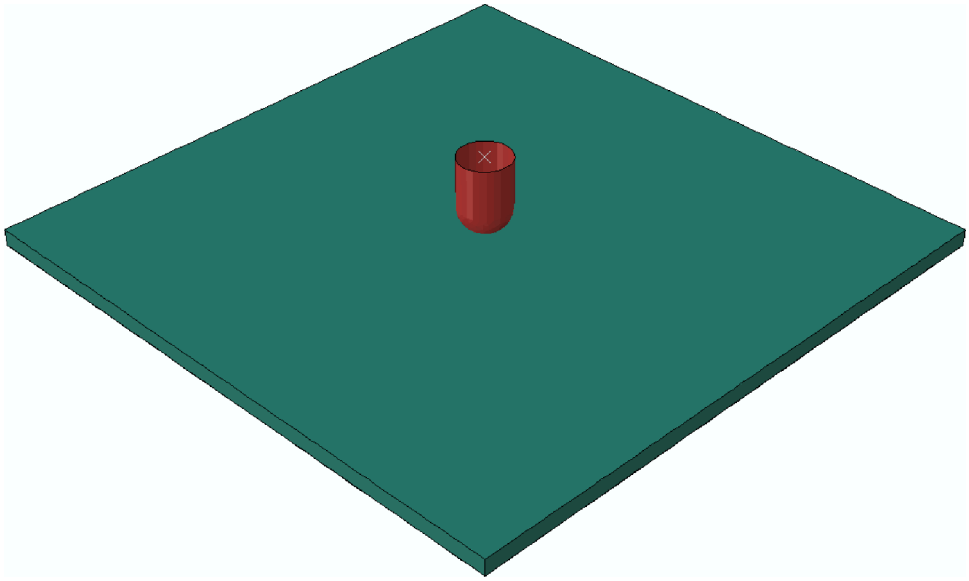

Fig. 10. Drop-weight finite element model.

Table 4
Fibre and matrix properties.

	Elastic Moduli		Shear Modulus	Poisson's ratio
	E_{f1}(GPa)	E_{f2}(GPa)	G_{f1}, G_m(GPa)	ν_{f1}, ν_m
Glass fibre	86.9	86.9	17.0	0.25
Carbon fibre	231.0	8.0	27.3	0.30
Matrix	2.9	2.9	1.1	0.35

Table 5
Ply elastic properties (Chamis' rule, [48]).

	Elastic Moduli (GPa)			Poisson's ratio		Shear Moduli (GPa)	
	E_1	E_2	E_3	ν_{12}	$\nu_{13} = \nu_{23}$	G_{12}	$G_{13} = G_{23}$
Glass layers	42.3	8.6	7.5	0.31	0.41	3.8	1.91
Carbon layers	110.1	5.2	7.5	0.32	0.42	4.2	1.95
Hybrid layer	85.1	6.4	7.5	0.32	0.42	4.1	1.93

Table 6
Ply strength (MPa) estimated from the Chamis' model, [48]).

	X_T	X_C	Y_T	Y_C	S_L	Z_C
Glass layers	2201	1980	68	109	40	400
Carbon layers	2237	1800	69	110	42	400
Hybrid layer	2206	1833	69	111	42	400

Table 7
Ply fracture toughness (N/mm) estimated from the elastic energy stored by each failure mode.

	G_{1+}	G_{1-}	G_{2+}	G_{2-}	G_6	G_{3-}
Glass layers	343	596	1	9	2	142
Carbon layers	127	94	1	8	1	153
Hybrid layer	207	280	1	8	1	149

results and requires less computational resources.

5.2. Geometry and constitutive model

The size of the laminate was 145×145 mm^2, whereas the test rig was modeled as a hollow square plate of 127×127 mm^2. The test rig was modeled as a rigid surface and the projectile was defined as a rigid body. The laminate was split into seven plies of the same thickness (0.586 mm). The shape of the impactor was hemispherical of 12.7 mm of diameter and 18.75 mm of height (Fig. 10).

Each ply was modeled with linear solid elements (with either 6 or 8 nodes and reduced integration). Plies were then connected each other by using conforming meshes. The mesh was refined at the impact region to capture stress gradients, leading to approximately 750 000 elements. A non-structured meshing strategy was followed to reduce the damage localisation problems commonly observed in materials with softening [45]. This mesh also showed a lower hourglassing effect compared to a structured mesh (see Appendix B). Regarding z-yarns, as they only contribute to fracture toughness enhancement, they were not modelled explicitly.

The mechanical properties of each ply were homogeneous. The plies behaved as orthotropic solids in which the response is linear elastic up to the onset of the intralaminar damage by matrix or fibre failure. A continuum damage model based on a simplified version of the LaRCO4 failure criteria [46,47] was implemented as a user subroutine VUMAT in Abaqus Explicit. A maximum stress failure criterion was selected to trigger and control the damage evolution variables. Six failure functions, including an out-of-plane compressive failure criteria, are defined: ϕ_{1+}, ϕ_{1-}, ϕ_{2+}, ϕ_{2-}, ϕ_6 and ϕ_{3-}.

$$longitudinaltension: \quad F_{1+} = \phi_{1+} - r_{1+} = \frac{E_1}{X_T}\varepsilon_1 - r_{1+}$$

$$longitudinalcompression: \quad F_{1-} = \phi_{1-} - r_{1-} = \frac{E_1}{X_C}\varepsilon_1 - r_{1-}$$

$$transversetension: \quad F_{2+} = \phi_{2+} - r_{2+} = \frac{E_2}{Y_T}\varepsilon_2 - r_{2+}$$

$$transversecompression: \quad F_{2-} = \phi_{2-} - r_{2-} = \frac{E_2}{Y_C}\varepsilon_2 - r_{2-}$$

$$in-planeshear: \quad F_6 = \phi_6 - r_6 = \frac{|S_{12}|}{S_L} - r_6$$

$$out-of-planecompression: \quad F_{3-} = \phi_{3-} - r_{3-} = \frac{|E_3|}{Z_C}\varepsilon_3 - r_{3-}$$

where X_T is the longitudinal tensile strength; X_C the longitudinal compressive strength; Y_T the transverse tensile strength; Y_C the in-plane transverse compressive strength; Z_C the out-of-plane compressive

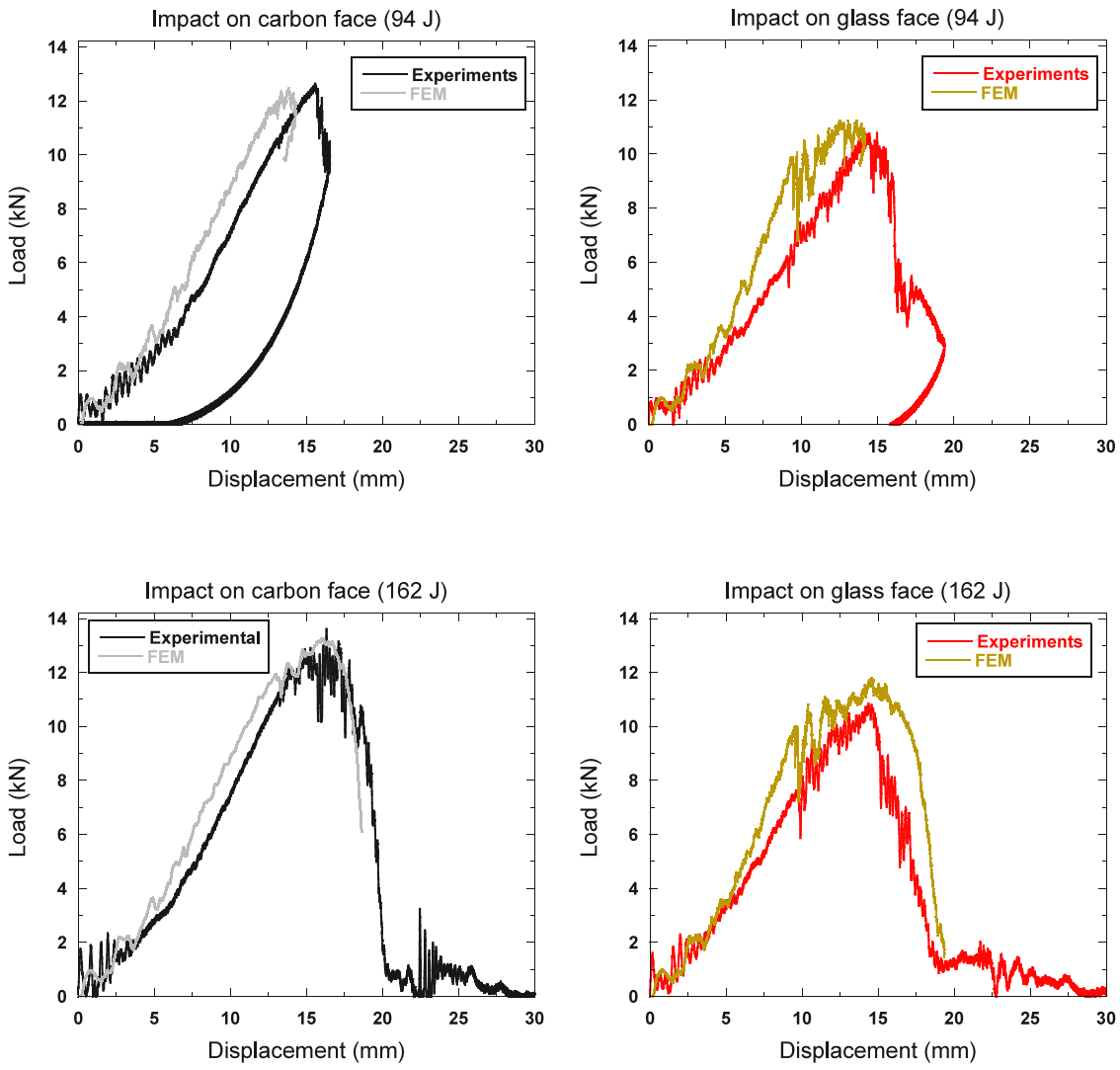

Fig. 11. Load-displacement curves corresponding to low velocity impacts without penetration (top) and with penetration (bottom). Comparison between computational and experimental results. To reduce computational cost, simulations were aborted once the tendency was well-defined.

strength and S_L the in-plane shear strength. r_i are the internal variables controlling damage evolution.

The input parameters of the constitutive model are the elastic constants (E_1, E_2, E_3, ν_{12}, ν_{13}, ν_{23}, G_{12}, G_{13}, G_{23}), the strengths (X_T, X_C, Y_T, Y_C, S_L, Z_C) and the fracture energies corresponding to each failure mode (G_{1+}, G_{1-}, G_{2+}, G_{2-}, G_6 and G_{3-}).

The elastic constants were determined by applying the micromechanical equations of Chamis [48] (see Tables 4 and 5). It was assumed that the stiffness in the through-thickness direction was similar to that in the transverse direction, so it was arbitrarily set to $E_3 = 7.5$ GPa. Chamis' equations were also applied to calculate the ply strengths (Table 6) from the fibre and matrix strengths provided by the manufacturers, except the through-thickness strength, which was also defined arbitrarily as $Zc = 400$ MPa.

The fracture toughness G_M, which is the product of the energy dissipated per unit volume g_M and the characteristic length l^* of the finite element, was first estimated as four times the elastic energy stored in each failure mode and then slightly tweaked to fit the load-displacement curve of the 94 J CF case. These values, which are presented in Table 7, were further used for the rest of the load cases. Note that fracture energies were sufficiently high to avoid snap-back[1] of the elements, [50].

Damage variables d_M were computed as a function of damage thresholds r_M:

$$d_M = 1 - \frac{1}{r_M} exp[A_M(1 - r_M)] \tag{5}$$

where M stands for the corresponding damage mechanisms ($1+$, $1-$, $2+$, $2-$, 6, $3-$).

The coefficients A_M are softening parameters that can be used to ensure mesh objectivity of the model, i.e., the models should dissipate the same amount of energy during failure independently of the size of the finite element discretisation.

5.3. Eroding criteria

Penetration modelling of continuum solids using finite element

[1] Snap-back occurs in brittle failures when the control of the load is lost, leading to an unstable solution that will dissipate more energy than it should, [45,49].

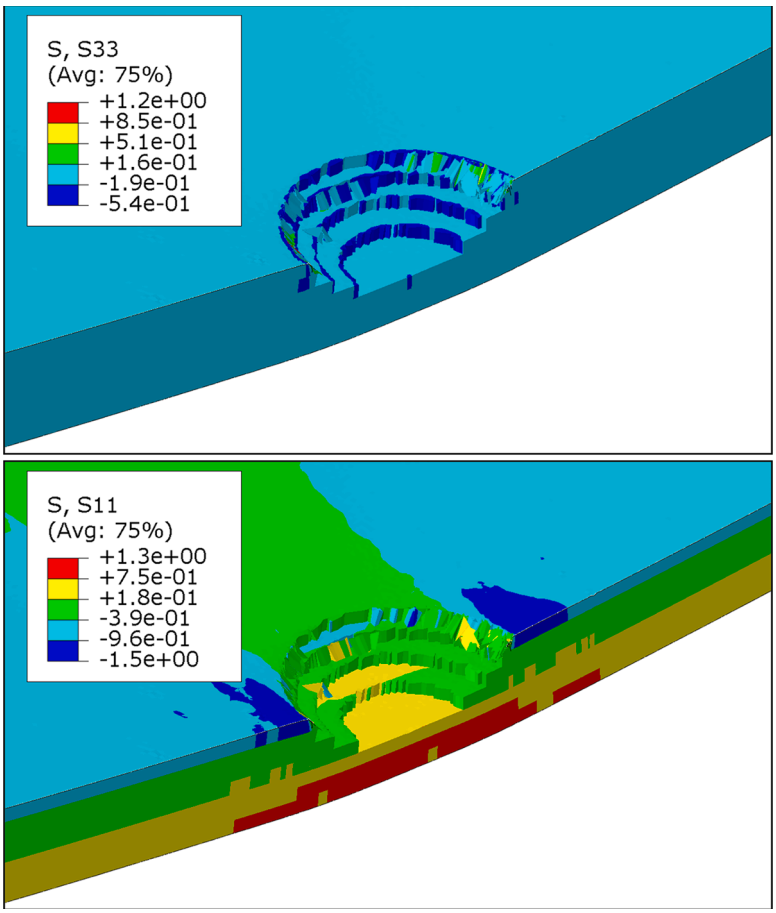

Fig. 12. Simulation of drop-weight impact of 94 J on carbon face. Footprint left at top layers of the laminate at time $t = 2.9$ ms. Contour plots indicate (top) out-of-plane compressive σ_{33} and (bottom) longitudinal (σ_{11}) stresses.

analysis requires an element erosion criteria to remove damaged elements with excessive deformation. The removal of an element generates traction-free surfaces and allows the penetrator to progress through the material, [51]. The influence of the erosion criteria on the mechanical response of the laminate was remarkable. In this case, elements were deleted after full degradation in tension in the fibre direction or in compression in the out-of-plane direction (crushing). Fibre breakage and crushing are controlled by the damage variables d_{1+} and d_{3-}, respectively. Actually, to avoid the distortion of elements and to reduce the computational cost of the simulations without affecting the results, failure cut-offs were defined at $d_1 = 0.7$ and $d_3 = 0.9$, before complete degradation occurs. Previous analyses showed that when the eroding criteria was defined in terms of the damage variables d_1 (fibre breakage) and either d_2 (transverse matrix cracking) or d_6 (in-plane shear cracking), the response became excessively compliant. This can be explained by the ability of the composites to withstand further loading after matrix cracking. Likewise, when d_1 was the only damage variable included in the erosion criteria, the response became too stiff and the impactor was unable to penetrate the laminate, which ended up failing only by bending.

5.4. Boundary conditions

The laminate was simply supported on the test rig, which was fully constrained so it was unable to translate or rotate. A normal contact was defined between laminate and rig to avoid penetration. The impactor was modeled as a rigid body and enforced to move along vertical direction with a mass point of 11.72 kg (94 J) and 22.4 kg (162 J) attached to it. Initial velocity of the impactor varied from 3.8 to 4.0 m/s. Since some elements may be removed during perforation, contact surfaces were defined in each ply.

5.5. Forward-Euler integration

Impacts were simulated by using the finite element code Abaqus Explicit. The Dynamic Explicit solver integrates the equations of motion by using an explicit central difference integration rule which satisfies the dynamic equilibrium at the beginning of an increment and calculates the kinematic state at the increment $i + 1$, [52]. As expected, the onset of damage clearly penalizes the critical stable time Δt, increasing the computational cost. Thus, simulations were aborted once the tendency of the unloading curve was identified. Although mass scaling could have been used to increase Δt, this approach was disregarded as it affects the energy balance and distorts the results. The distortion control option, which prevents solid elements from inverting, was also disregarded due to the non-negligible artificial energy introduced in the model.

6. Computational results and comparison with experiments

A good agreement was found between experiments and simulations. As shown in the load-displacement curves depicted in Fig. 11, the FE model was able to capture the differences between the CF and the GF configurations, as well as the energy required to perforate the laminate. Correlation was better in specimens impacted on the carbon face. The stiffness of the GF configuration was overestimated, probably due to the modelling strategy, which does not account for tow sliding. In contrast, peak loads, which are mainly controlled by the fibre strength, were well estimated in both configurations.

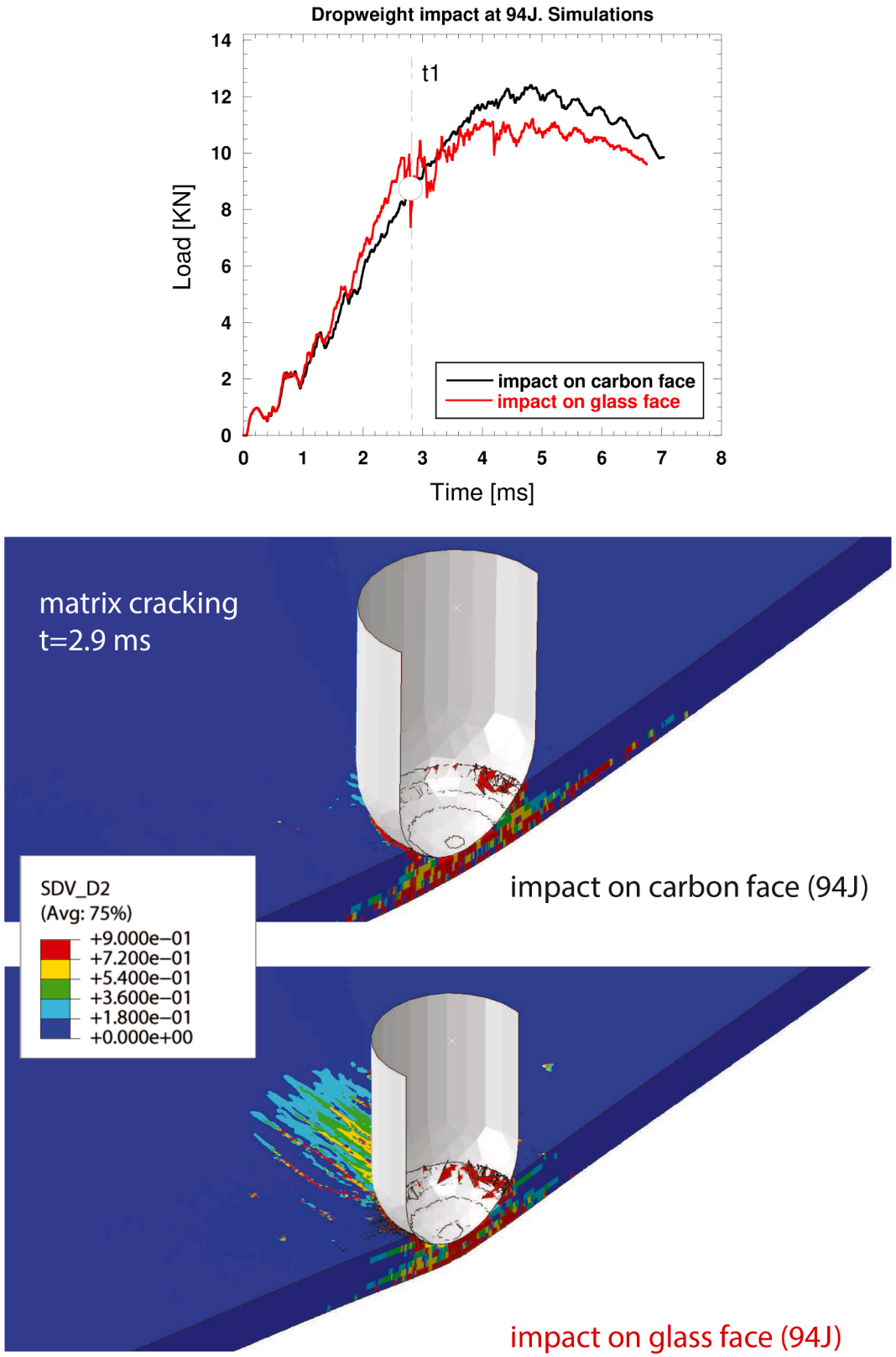

Fig. 13. Simulation of dropweight impact of 94 J on carbon (top) and glass (bottom) faces at time $t_1 = 2.9$ ms. Contour plots indicate the damage level for matrix cracking.

It is worth noting that most of the low-velocity impact modelling approaches found in the literature have been validated based on the force-time curves of low impact energies in which the mechanical behaviour of the composite is mainly dominated by the elastic properties of the components [53–55]. In this study, we compared the load-displacement curves and damage patterns for impact energies causing even perforation, which makes it particularly challenging.

Once the FE model was validated, it was used to explain the damage

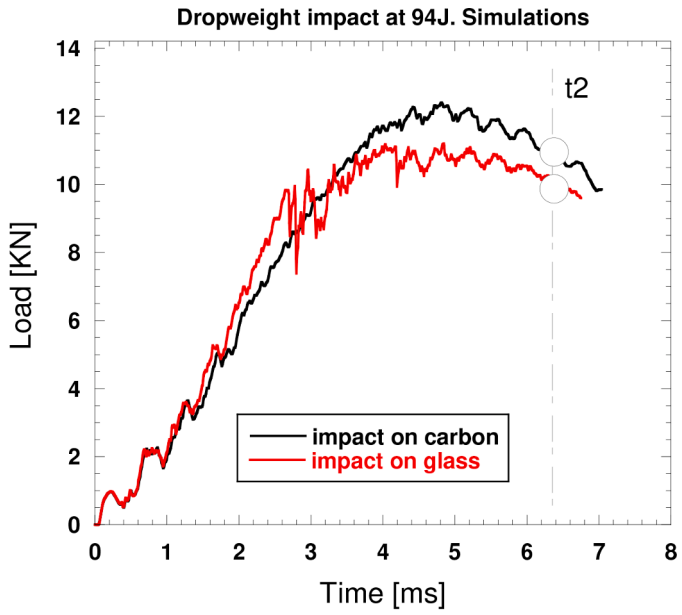

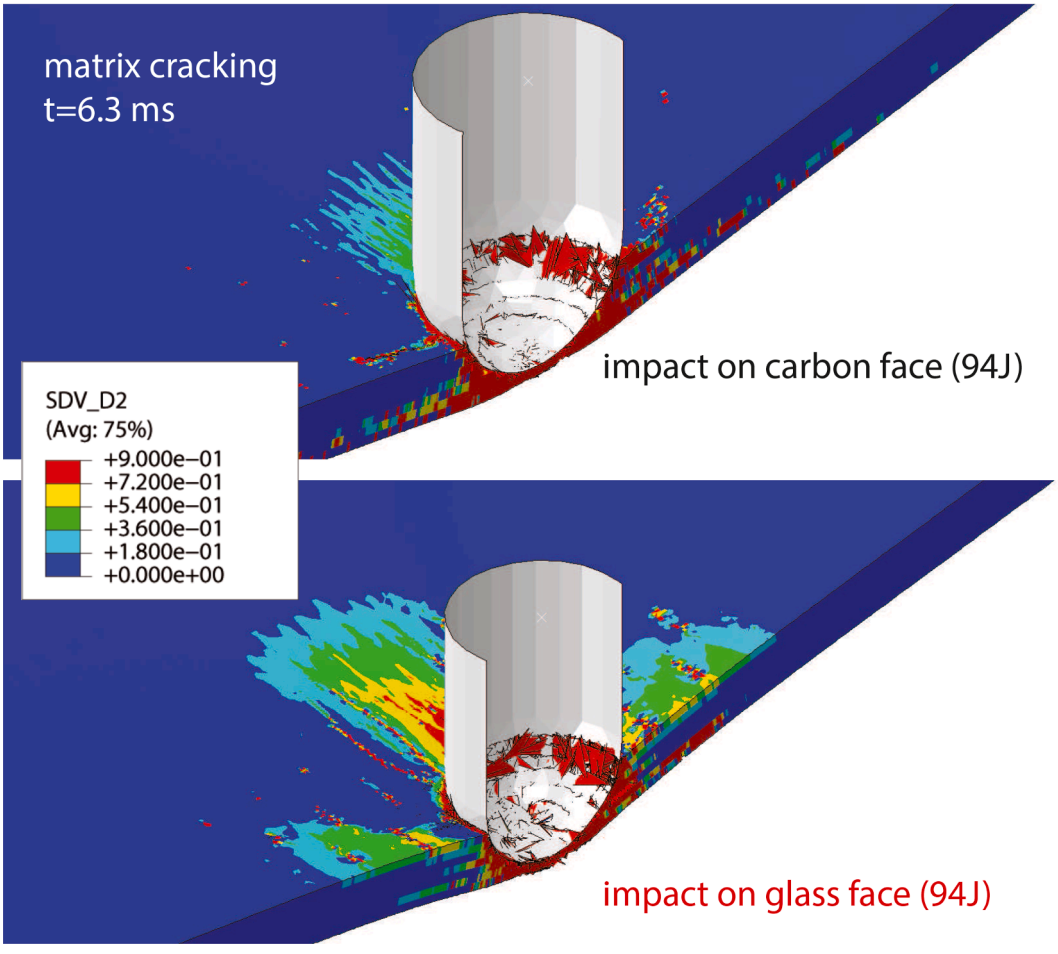

Fig. 14. Simulation of drop-weight impact of 94 J on carbon (top) and glass (bottom) faces at time $t_2 = 6.3$ ms. Contour plots indicate the damage level corresponding to matrix cracking.

evolution. As the impactor comes into contact with the top layer of the laminate, contact pressure exceeds the out-of-plane compressive strength of the material and elements are automatically deleted by crushing ($d_{3\_}$). This enables the impactor to *bite* progressively the top layers. As shown in Fig. 12, at time $t_1 = 2.9$ ms 4 layers had been removed. Simultaneously, global plate bending gives rise to significant tensile stresses at the back layers, which further promotes impactor penetration. The process was accompanied with significant transverse and in-plane shear matrix cracking (Fig. 13).

At time $t_2 = 6.3$ ms there was significant matrix damage in all layers

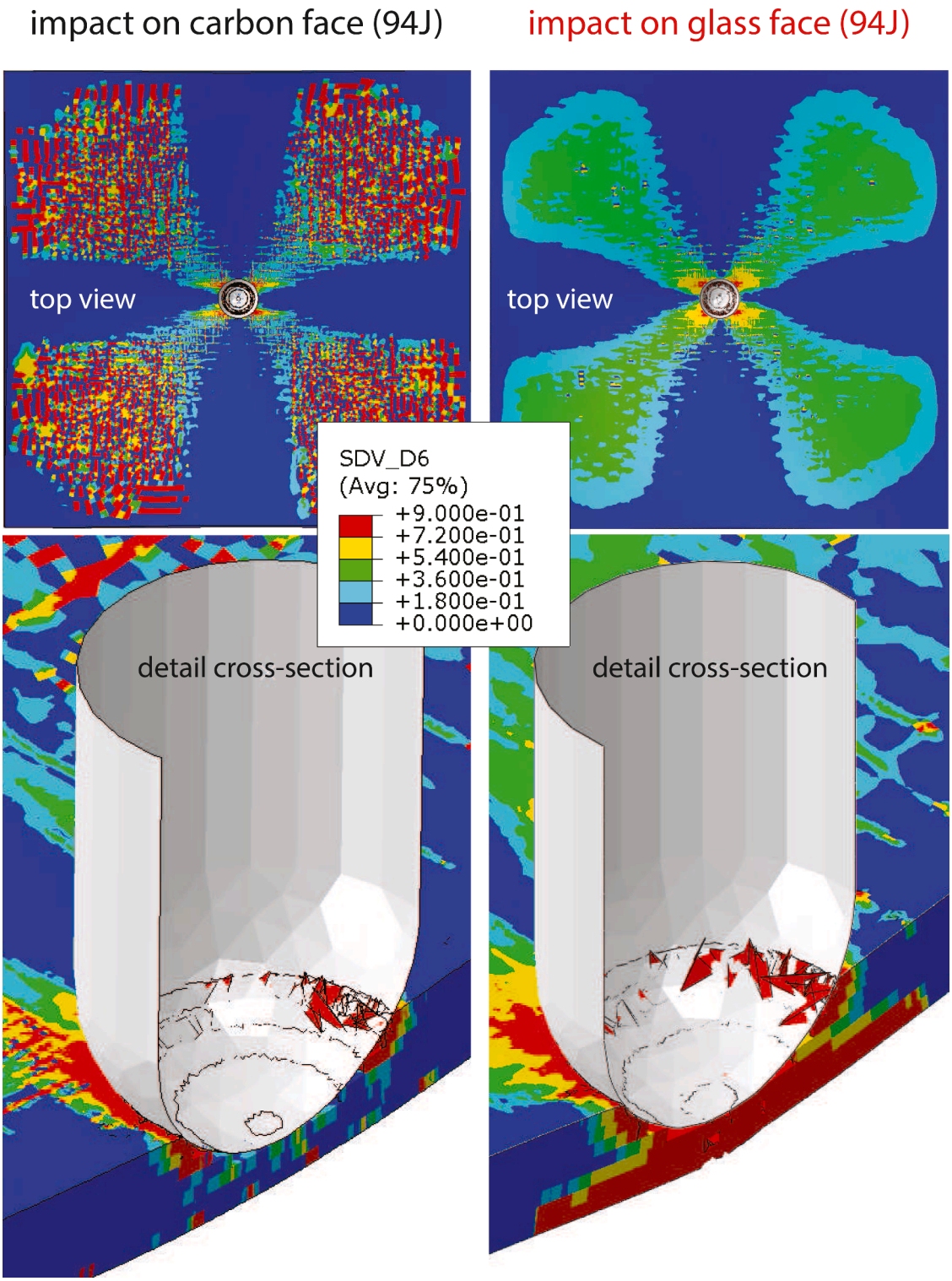

Fig. 15. Simulation of drop-weight impact of 94 J on (left) carbon and (right) glass faces. Contour plots indicate the damage level corresponding to in-plane shear cracking at $t_1 = 2.9$ ms. Details of the impacted region are shown at the bottom.

(Figs. 14 and 15), but that was not sufficient to cause fibre breakage at the back layer. This explains why the impactor eventually rebounded. The FE model perfectly captures that GF was almost perforated at $t_2 = 6.3$ ms, which is in agreement with experimental results.

At higher impact energies (162 J), the impact sequence was similar, except that fibre breakage of the back layer eventually occurred, allowing the perforation of the laminate (Fig. 16). This is also in agreement with experimental results.

Comparison between CF and GF configurations revealed that bending and both matrix and fibre damage were greater on GF, regardless of the impact energy. The higher failure strain of the glass fibres located at the bottom ensures higher energy absorption during bending, and explains the differences between the GF and CF configurations.

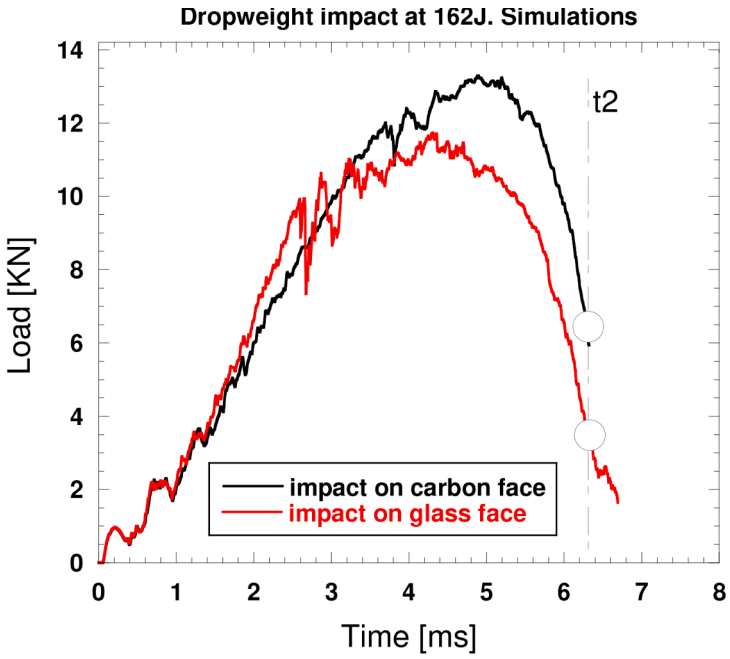

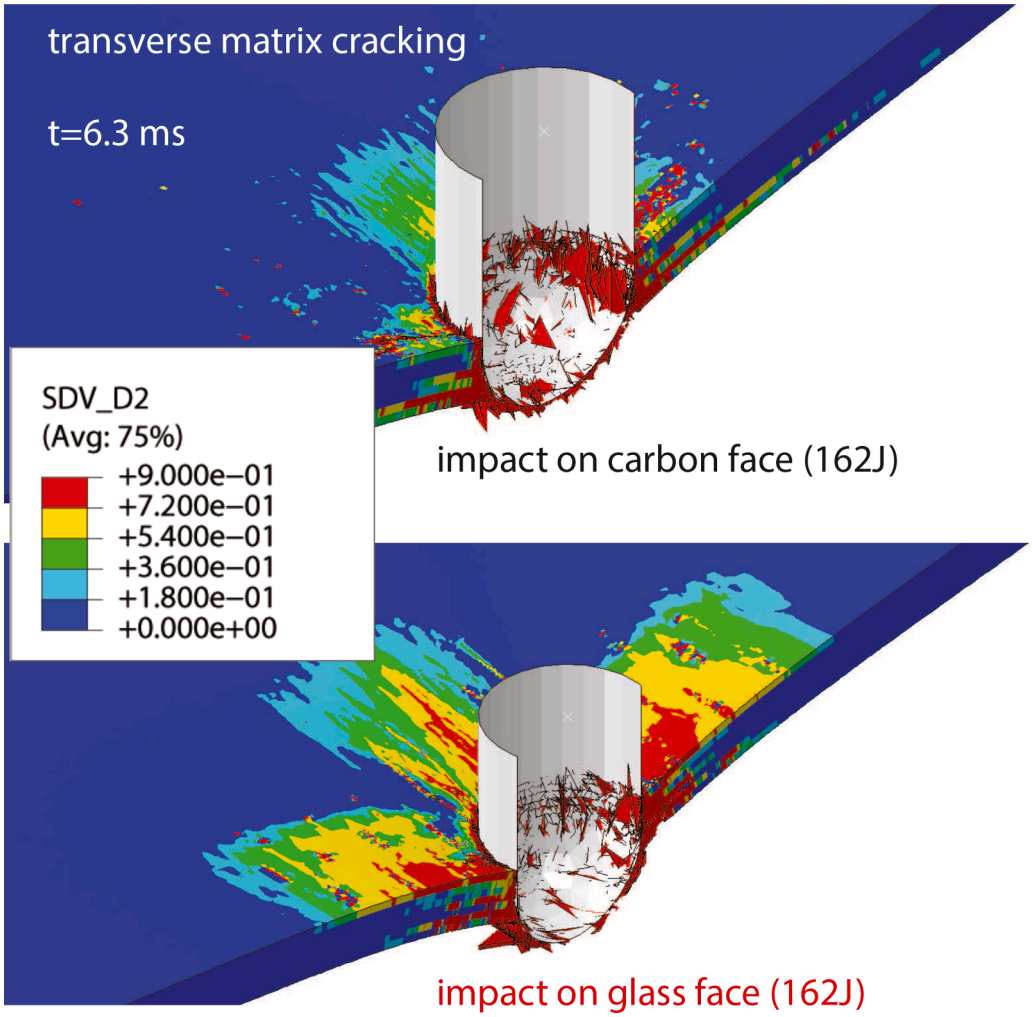

Fig. 16. Simulation of drop-weight impact of 162 J on carbon and glass faces. Contour plots indicate the matrix damage level corresponding to matrix cracking at t_2 = 6.35 ms.

7. Conclusions

The mechanical behaviour of a hybrid 3D woven composite was studied under low-velocity impact. The material exhibits a remarkable impact performance for aerospace applications mainly due to the presence of the through-thickness reinforcement, which gives rise to multiple failure mechanisms, enhancing energy dissipation and improving the impact performance of the material.

Significant differences were found in terms of energy absorption and damage depending on the impact face. The configuration CF (carbon fibres at the top and glass fibres at the bottom) provides the best performance at both impact energy levels. According to XCT observations and the FE analysis, this is due to the fact that final failure of coupons is mainly controlled by fibre breakage, which in turn depends on the normal stresses caused by plate bending. As failure strain of s2-glass fibres is much higher than that of carbon fibres, the laminate can withstand higher deformation when glass fibres are located at the bottom. The CF configuration undergoes a much smoother deformation process than the GF configuration (glass fibres at the top and carbon fibres at the bottom), where damage is more localised around the impactor.

Finite Element Analysis has been used to reproduce the experimental results. The constitutive model of each ply is based on a relatively simple maximum stress failure criteria. Despite of the complexity of the 3D preform and the multiple failure mechanisms involved during the damage process, simulations suggest that the mechanical behaviour of the composite is still controlled by the stiffness, the strength and the fracture toughness of the plies. This suggest that 3D woven composites can be modelled using similar strategies than those of unidirectional laminates, such as homogenisation of ply properties and the use of continuum damage mechanics. Modelling should account for the knock-down factors in the in-plane mechanical properties, the higher fracture toughness of 3D woven composites and the need of an out-of-plane compressive failure criterion. An appropriate eroding criteria must also be defined to enable progressive erosion of the material.

The FE model presented here is capable of predicting reasonably well the energy absorbed, the peak force and the load-displacement curves, which are more challenging than force-time curves, especially at high impact energy levels. However, the modelling strategy presented here is only valid for simulating the impact behaviour of 3D woven composites in which delamination has been fully suppressed.

The simulations helped to understand the failure mechanisms involved and also to predict how hybridisation can improve impact energy absorption.

CRediT authorship contribution statement

Raúl Muñoz: Writing – original draft, Methodology, Software, Visualization, Investigation, Formal analysis. **Rocío Seltzer:** Writing – original draft, Investigation. **Federico Sket:** Investigation, Methodology. **Carlos González:** Supervision, Conceptualization, Project administration, Writing – review & editing, Funding acquisition. **Javier Llorca:** Supervision, Writing – review & editing, Funding acquisition.

Declaration of Competing Interest

The authors have no conflicts of interest to disclose.

Acknowledgments

The authors kindly acknowledge the support of the Spanish Ministry of Economy and Competitiveness through the project MAT2012-37552.

Appendix A. Modelling with cohesive and truss elements

This appendix presents an alternative modelling strategy of 3D composites that includes cohesive elements (delamination) and truss elements (z-yarns).

Each ply is modelled with solid elements, as explained in section *Computational Model*. The main two differences with the modelling strategy presented in the main text is that delamination is taken into account with three-dimensional cohesive elements (COH3D8) and the through-thickness effect of the PE z-yarns is introduced in the FE model by means of linear truss elements (T3D2). The meshes corresponding to the embedded (truss) and host elements (solid & cohesive) are superimposed (Fig. 17), and a kinematic relationship is established between them. When a node of an embedded element lies within a host element, the translational degrees of freedom of the embedded node are constrained to the interpolated values of the corresponding degrees of freedom of the host element. The main advantage of the embedded element technique, which is available in Abaqus Explicit, is that nodes from the host and the embedded elements are not necessarily coincident (Fig. 18). Further details can be found in [44].

The constitute model of cohesive elements is defined by a traction-separation law in which damage initiation is controlled by a quadratic strength-based criterion. The z-yarns were assumed to behave as linear elastic materials. Failure in tension was triggered at critical fracture stress and was followed by a progressive reduction in the load carried by the z-yarn, which depends on the fracture energy associated with the fracture of the PE z-yarns.

The mechanical properties of the z-yarns were calculated from the fibre diameter, the areal density and yarn spacing, which were provided by the manufacturer. The linear density of the z-yarn is the ratio of the areal density ($74.6 \cdot 10^{-6}$ g/mm^2) and yarn spacing (0.3937 yarns/mm). This is divided by the linear density of the fibres ($3.36 \cdot 10^{-7}$ g/mm), resulting in a total of 564 fibres. As the diameter of the PE fibres is known (21 μm), the resulting dry cross section is $\pi \frac{(21 \cdot 10^{-3})^2}{4} mm^2 \times 564 = 0.195 \text{mm}^2$.

Material properties of cohesive elements and z-yarns are collected in Tables 8 and 9.

Fig. 19 compares the load-displacement curve of the modelling strategy presented in this appendix with that of the main text. Results indicate that the presence of cohesive elements causes an unrealistic reduction of stiffness at approximately 3.5 kN due to the onset of delamination. As shown in Fig. 20, truss elements slightly improved the mechanical behaviour, but it is still far from the experimental results. It is worth noting that delamination was not observed in the XCT analysis of the 3D woven composite studied in this paper.

It can be concluded that the modelling strategy presented in this appendix, that includes cohesive and truss elements, is not appropriate for simulating the impact behaviour of the hybrid 3D woven composite studied here. However, it might be useful for simulating 3D composites in which

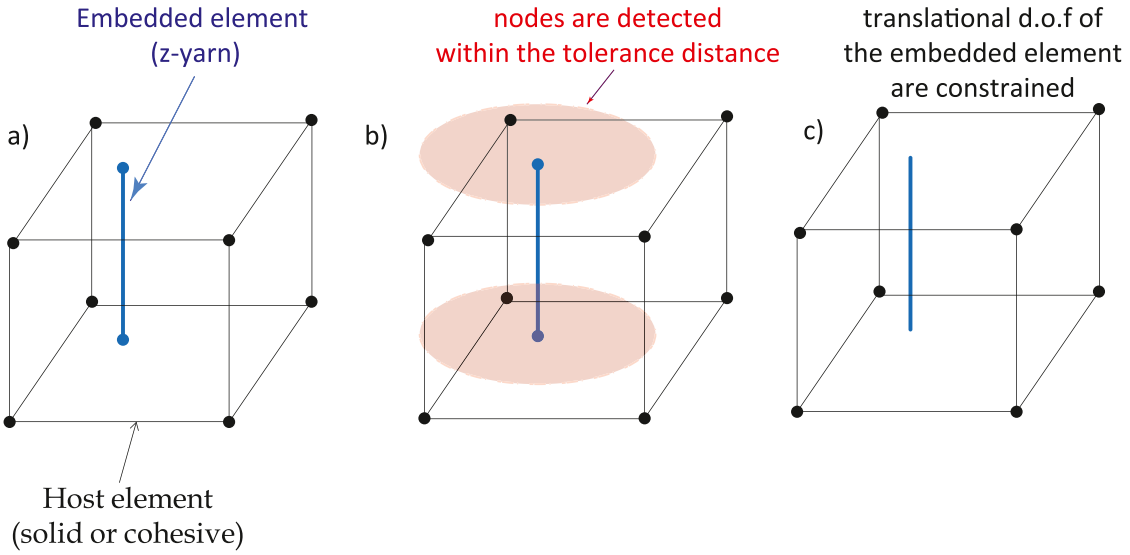

Fig. 17. Schematic representation of the embedded element technique.

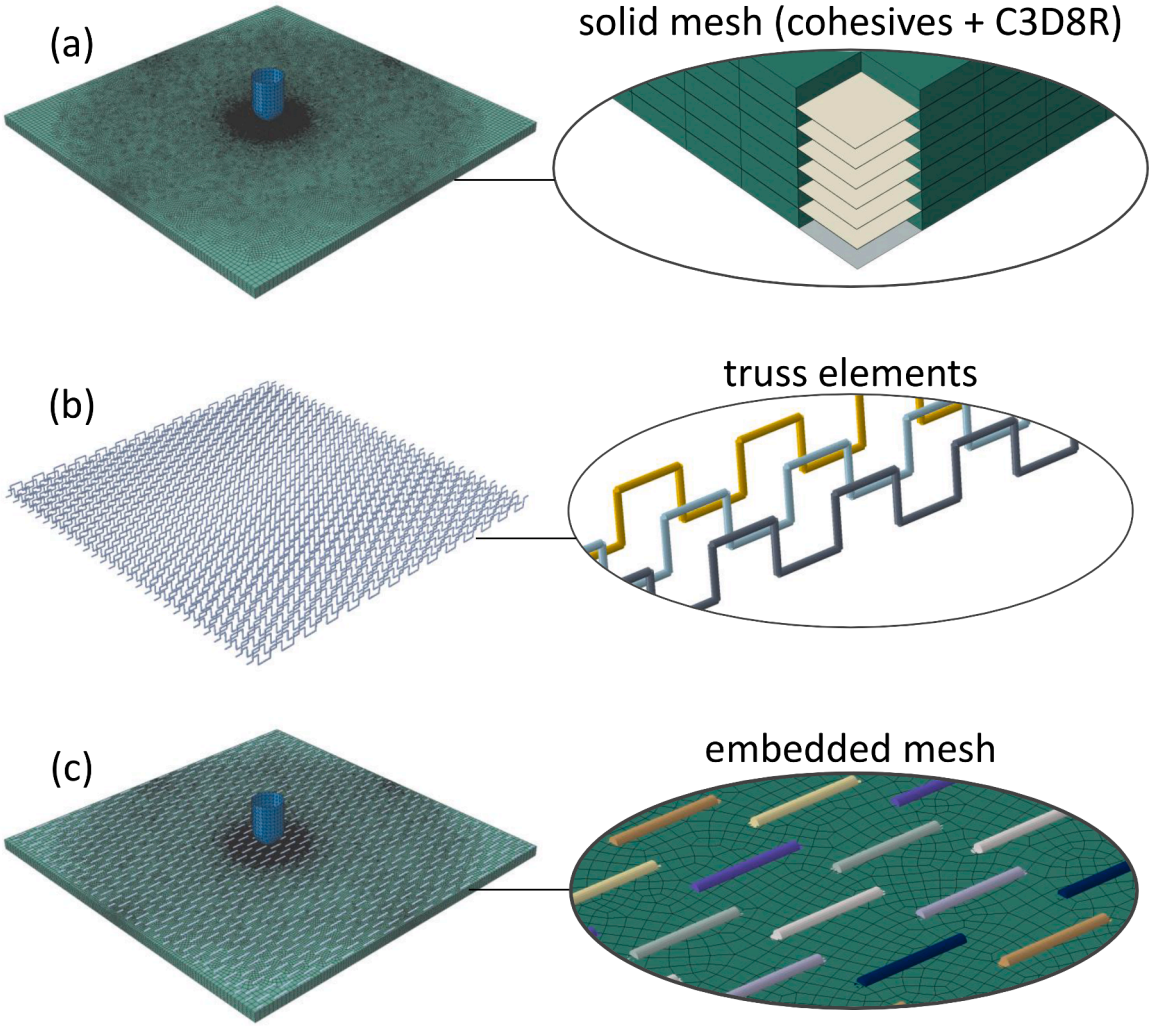

Fig. 18. Suggested modelling approach for 3D composites susceptible to delamination. (a) Solid mesh (hexaedral and cohesive elements) is combined with (b) truss elements by using the embedded element technique. The resulting mesh is illustrated in (c).

Table 8
Cohesive material properties.

Parameter	Value
Normal interface Strength, N (MPa)	53
Shear interface Strength, S (MPa)	104
Mode I fracture toughness, G_{Ic} (kJ/m^2)	0.3
Mode II fracture toughness, G_{IIc} (kJ/m^2)	0.8
Benzeggah-Kenane parameter, η	1.75

Table 9
Z-yarn properties.

Parameter	Value
Density (kg/m^3)	970
Cross sectional area (mm^2)	0.195
Elastic Modulus (GPa)	113
Poisson's ratio	0.275
Fracture stress (GPa)	0.55
Fracture energy (kJ/m^2)	11
Failure strain (%)	4

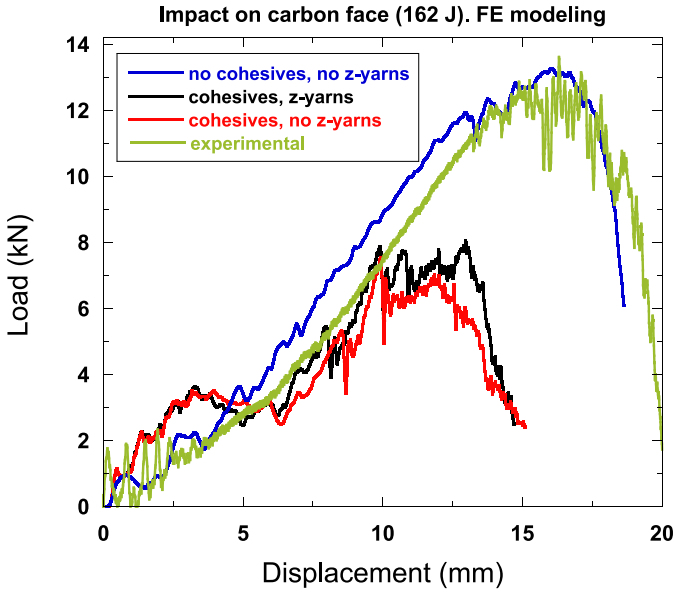

Fig. 19. Impact on carbon face at 162 J. Comparison of three modelling strategies with the experimental results: (red) cohesive elements and no z-yarns; (black) cohesive elements & z-yarns; (blue) no cohesive elements and no z-yarns. (For interpretation of the references to colour in this figure legend, the reader is referred to the web version of this article.)

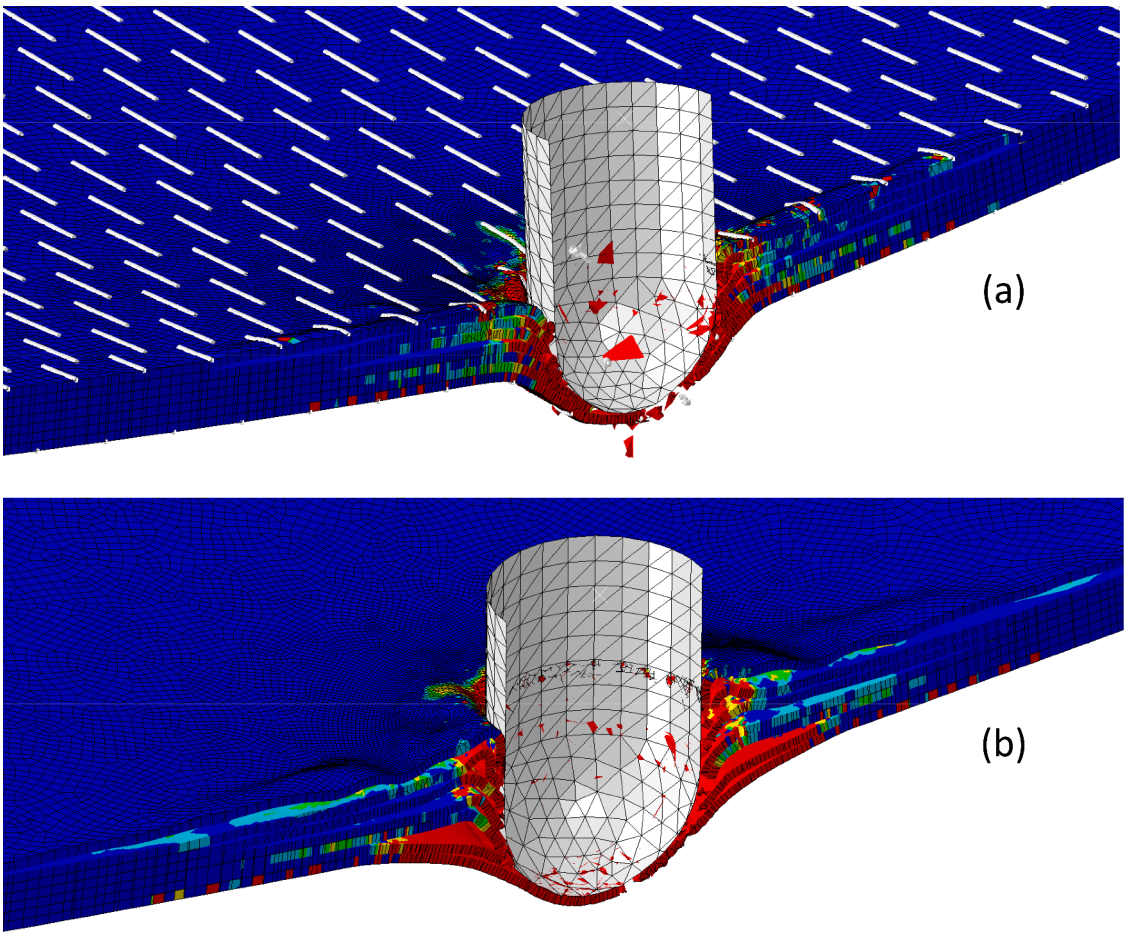

Fig. 20. Impact on carbon face at 162 J. (a) Simulation with cohesive and truss elements. (b) Simulation with cohesive elements.

delamination actually occurs, although further research is required.

Appendix B. Hourglassing

Linear reduced-integration elements, such as the one selected in this analysis (C3D8R), may suffer from a numerical problem called *hourglassing* that causes non-physical deformation. This phenomenon was observed when using a structured mesh (Fig. 22).

This can be avoided by using full integration and/or quadratic interpolation, but at the expense of a much higher computational cost and potential shear locking effects. Alternatively, finer meshes can limit the propagation of hourglassing modes, so we significantly reduced the element size at the impact region. To ensure a smooth transition between small and large elements, the structured mesh was replaced by a non-structured one, resulting in no hourglass propagation and a significant reduction of the artificial energy. As shown in Fig. 23, the structured mesh requires approximately four times more artificial energy than the unstructured mesh. The artificial energy (ALLAE) of the unstructured mesh is approximately 7.5% of the total internal energy (ALLIE).

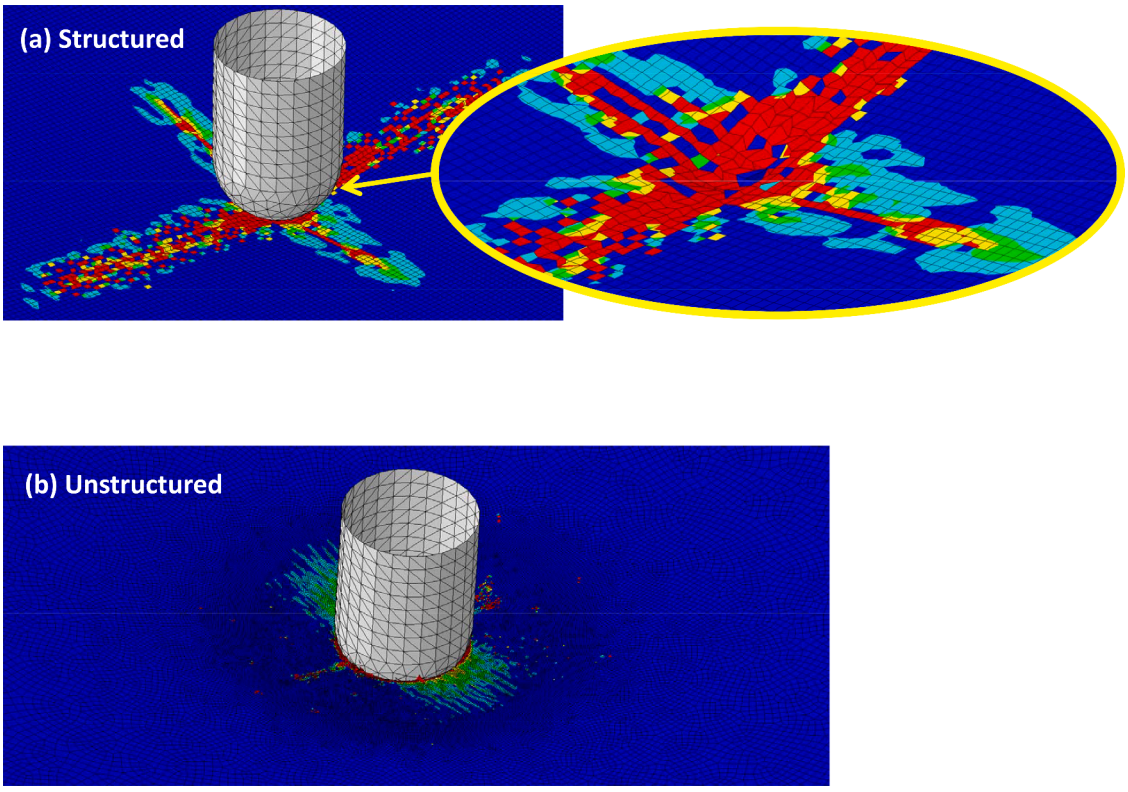

Fig. 22. (a) The structured mesh exhibits hourglassing mode propagation; (b) Unstructured mesh enabled us to reduce the element size at the impact region and thus avoid hourglassing.

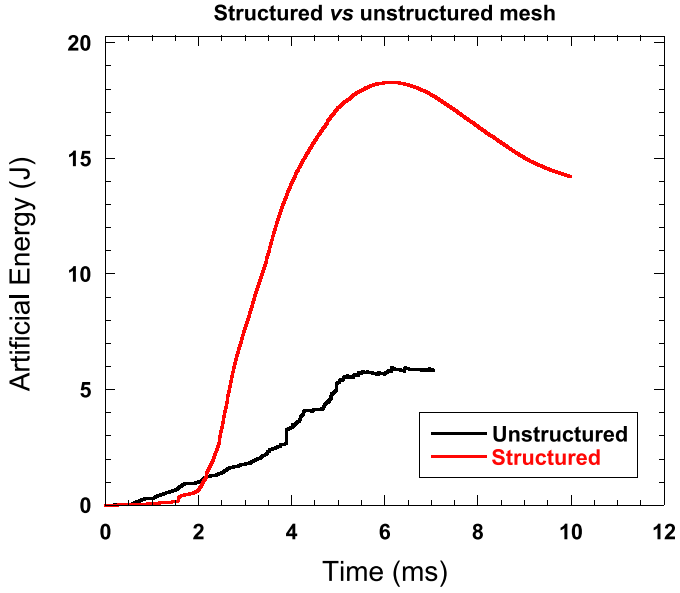

Fig. 23. Evolution of the artificial energy (ALLAE) of the structured and unstructured meshes during impact loading.

References

[1] Rhymer J, Kim H, Roach D. The damage resistance of quasi-isotropic carbon/epoxy composite tape laminates impacted by high velocity ice. Comp Part A 2012;43(7):1134–44. https://doi.org/10.1016/j.compositesa.2012.02.017.

[2] Dransfield K, Baillie C, Mai YW. Improving the delamination resistance of cfrp by stitching-a review. Compos Sci Technol 1994;50(3):305–17. https://doi.org/10.1016/0266-3538(94)90019-1.

[3] Beckermann GW, Pickering KL. Mode i and mode II interlaminar fracture toughness of composite laminates interleaved with electrospun nanofibre veils. Comp Part A 2015;72:11–21. https://doi.org/10.1016/j.compositesa.2015.01.028.

[4] Nash N, Young T, McGrail P, Stanley W. Inclusion of a thermoplastic phase to improve impact and post-impact performances of carbon fibre reinforced thermosetting composites - a review. Mater Des 2015;85:582–97. https://doi.org/10.1016/j.matdes.2015.07.001.

[5] van der Heijden S, Daelemans L, De Schoenmaker B, De Baere I, Rahier H, Van Paepegem W, et al. Interlaminar toughening of resin transfer moulded glass fibre

epoxy laminates by polycaprolactone electrospun nanofibres. Compos Sci Technol 2014;104:66–73. https://doi.org/10.1016/j.compscitech.2014.09.005.
[6] Aljarrah MT, Abdelal NR. Improvement of the mode i interlaminar fracture toughness of carbon fiber composite reinforced with electrospun nylon nanofiber. Comp Part B 2019;165:379–85. https://doi.org/10.1016/j.compositesb.2019.01.065.
[7] Göktaş D, Kennon WR, Potluri P. Improvement of mode i interlaminar fracture toughness of stitched glass/epoxy composites. Appl Compos Mater 2017;24(2):351–75. https://doi.org/10.1007/s10443-016-9560-x.
[8] Tan K, Yoshimura A, Watanabe N, Iwahori Y, Ishikawa T. Effect of stitch density and stitch thread thickness on damage progression and failure characteristics of stitched composites under out-of-plane loading. Compos Sci Technol 2013;74:194–204. https://doi.org/10.1016/j.compscitech.2012.11.001.
[9] Cartié D, Cox B, Fleck N. Mechanisms of crack bridging by composite and metallic rods. Comp Part A 2004;35(11):1325–36. https://doi.org/10.1016/j.compositesa.2004.03.006.
[10] Warzok F, Allegri G, Gude M, Hallett S. Experimental characterisation of fatigue damage in single z-pins. Comp Part A 2016;91:461–71. https://doi.org/10.1016/j.compositesa.2016.03.023.CompTest 2015
[11] Mouritz A. Review of z-pinned composite laminates. Comp Part A 2007;38(12):2383–97. https://doi.org/10.1016/j.compositesa.2007.08.016.
[12] Neale G, Dahale M, Yoo S, Toso N, McGarrigle C, Quinn J, Kelly J, McIlhagger A, Archer E, Harkin-Jones E. Improved crush energy absorption in 3d woven composites by pick density modification. Comp Part B 2020;192:108007. https://doi.org/10.1016/j.compositesb.2020.108007.
[13] Khokar N. 3D-weaving: theory and practice. J Textile Instit 2001;92(2):193–207. https://doi.org/10.1080/00405000108659570.
[14] Saleh MN, Soutis C. Recent advancements in mechanical characterisation of 3d woven composites. Mech Adv Mater Modern Process 2017;3(1):12. https://doi.org/10.1016/j.compstruct.2011.03.010.
[15] Stegschuster G, Pingkarawat K, Wendland B, Mouritz A. Experimental determination of the mode i delamination fracture and fatigue properties of thin 3d woven composites. Comp Part A 2016;84:308–15. https://doi.org/10.1016/j.compositesa.2016.02.008.
[16] Potluri P, Hogg P, Arshad M, Jetavat D, Jamshidi P. Influence of fibre architecture on impact damage tolerance in 3d woven composites. Appl Compos Mater 2012;19(5):799–812. https://doi.org/10.1007/s10443-012-9256-9.
[17] Goud V, Singh D, Ramasamy A, Das A, Kalyanasundaram D. Investigation of the mechanical performance of carbon/polypropylene 2d and 3d woven composites manufactured through multi-step impregnation processes. Comp Part A 2020;130:105733. https://doi.org/10.1016/j.compositesa.2019.105733.
[18] Hart KR, Chia PX, Sheridan LE, Wetzel ED, Sottos NR, White SR. Mechanisms and characterization of impact damage in 2d and 3d woven fiber-reinforced composites. Comp Part A 2017;101:432–43. https://doi.org/10.1007/s10443-012-9256-9.
[19] Saleh MN, El-Dessouky HM, Saeedifar M, De Freitas ST, Scaife RJ, Zarouchas D. Compression after multiple low velocity impacts of ncf, 2d and 3d woven composites. Comp Part A 2019;125:105576. https://doi.org/10.1016/j.compositesa.2019.105576.
[20] Chocron S, Carpenter AJ, Scott NL, Bigger RP, Warren K. Impact on carbon fiber composite: ballistic tests, material tests, and computer simulations. Int J Impact Eng 2019;131:39–56. https://doi.org/10.1016/j.ijimpeng.2019.05.002.
[21] Seltzer R, González C, Muñoz R, LLorca J, Blanco-Varela T. X-Ray microtomography analysis of the damage micromechanisms in 3d woven composites under low-velocity impact. Comp Part A 2013;45:49–60. https://doi.org/10.1016/j.compositesa.2012.09.017.
[22] Swolfs Y, Gorbatikh L, Verpoest I. Fibre hybridisation in polymer composites: a review. Comp Part A 2014;67:181–200. https://doi.org/10.1016/j.compositesa.2014.08.027.
[23] Safri SNA, Sultan MTH, Jawaid M, Jayakrishna K. Impact behaviour of hybrid composites for structural applications: a review. Comp Part B 2018;133:112–21. https://doi.org/10.1016/j.compositesb.2017.09.008.
[24] Silva M, Santos P, Parente J, Valvez S, Reis P. Hybridization effect on the impact properties of flax composites. Procedia Struct Integrity 2020;28:2235–44. https://doi.org/10.1016/j.prostr.2020.11.052.1st Virtual European Conference on Fracture - VECF1
[25] Yang Y, Chen X. Investigation on energy absorption efficiency of each layer in ballistic armour panel for applications in hybrid design. Compos Struct 2017;164:1–9. https://doi.org/10.1016/j.compstruct.2016.12.057.
[26] Sevkat E, Liaw B, Delale F. Drop-weight impact response of hybrid composites impacted by impactor of various geometries. Mater Des (1980–2015) 2013;52:67–77. https://doi.org/10.1016/j.matdes.2013.05.016.
[27] Papa I, Boccarusso L, Langella A, Lopresto V. Carbon/glass hybrid composite laminates in vinylester resin: bending and low velocity impact tests. Compos Struct 2020;232:111571. https://doi.org/10.1016/j.compstruct.2019.111571.
[28] Shah S, Karuppanan S, Megat-Yusoff P, Sajid Z. Impact resistance and damage tolerance of fiber reinforced composites: a review. Compos Struct 2019;217:100–21. https://doi.org/10.1016/j.compstruct.2019.03.021.
[29] Ribeiro F, Sena-Cruz J, Vassilopoulos AP. Tension-tension fatigue behavior of hybrid glass/carbon and carbon/carbon composites. Int J Fatigue 2021;146:106143. https://doi.org/10.1016/j.ijfatigue.2021.106143.
[30] Bandaru AK, Vetiyatil L, Ahmad S. The effect of hybridization on the ballistic impact behavior of hybrid composite armors. Comp Part B 2015;76:300–19. https://doi.org/10.1016/j.compositesb.2015.03.012.
[31] Enfedaque A, Molina-Aldareguía J, Gálvez F, González C, LLorca J. Effect of glass fiber hybridization on the behavior under impact of woven carbon fiber/epoxy laminates. J Compos Mater 2010;44(25):3051–68. https://doi.org/10.1177/0021998310369602.
[32] Abrate S. Impact on composite structures. Cambridge University Press; 1998. https://doi.org/10.1017/CBO9780511574504.
[33] González EV, Maimí P, Camanho PP, Lopes CS, Blanco N. Effects of ply clustering in laminated composite plates under low-velocity impact loading. Compos Sci Technol 2011;71(6):805–17. https://doi.org/10.1016/j.compscitech.2010.12.018.
[34] Lopes C, Seresta O, Coquet Y, Gürdal Z, Camanho P, Thuis B. Low-velocity impact damage on dispersed stacking sequence laminates. part i: experiments. Compos Sci Technol 2009;69(7):926–36. https://doi.org/10.1016/j.compscitech.2009.02.009.
[35] Caprino G, Lopresto V, Scarponi C, Briotti G. Influence of material thickness on the response of carbon-fabric/epoxy panels to low velocity impact. Compos Sci Technol 1999;59(15):2279–86. https://doi.org/10.1016/S0266-3538(99)00079-2.
[36] Kazemianfar B, Esmaeeli M, Nami MR. Response of 3d woven composites under low velocity impact with different impactor geometries. Aerosp Sci Technol 2020;102:105849. https://doi.org/10.1016/j.ast.2020.105849.
[37] Midani M, Seyam A-F, Saleh MN, Pankow M. The effect of the through-thickness yarn component on the in- and out-of-plane properties of composites from 3d orthogonal woven preforms. J Textile Instit 2019;110(3):317–27. https://doi.org/10.1080/00405000.2018.1481722.
[38] Castaneda N, Wisner B, Cuadra J, Amini S, Kontsos A. Investigation of the z-binder role in progressive damage of 3d woven composites. Comp Part A 2017;98:76–89. https://doi.org/10.1016/j.compositesa.2016.11.022.
[39] Muñoz R, Martínez V, Sket F, González C, LLorca J. Mechanical behavior and failure micromechanisms of hybrid 3d woven composites in tension. Comp Part A 2014;59:93–104. https://doi.org/10.1017/CBO9780511574504.
[40] Muñoz R, González C, Llorca J. Mechanisms of in-plane shear deformation in hybrid three-dimensional woven composites. J Compos Mater 2015;49(30):3755–63. https://doi.org/10.1016/j.compositesa.2014.01.003.
[41] Naouar N, Vidal-Salle E, Schneider J, Maire E, Boisse P. 3D composite reinforcement meso f.e. analyses based on x-ray computed tomography. Compos Struct 2015;132:1094–104. https://doi.org/10.1016/j.compstruct.2015.07.005.
[42] Green S, Matveev M, Long A, Ivanov D, Hallett S. Mechanical modelling of 3d woven composites considering realistic unit cell geometry. Compos Struct 2014;118:284–93. https://doi.org/10.1016/j.compstruct.2014.07.005.
[43] Zheng T, Guo L, Tang Z, Wang T, Li Z. Comparison of progressive damage simulation of 3d woven composites between voxel and conformal discretization models. Mech Mater 2021;158:103860. https://doi.org/10.1016/j.mechmat.2021.103860.
[44] Muñoz R, Martínez-Hergueta F, Gálvez F, González C, LLorca J. Ballistic performance of hybrid 3d woven composites: experiments and simulations. Compos Struct 2015;127:141–51. https://doi.org/10.1016/j.compstruct.2015.03.0210.
[45] Bažant PJ, P Z. Fracture and size effect in concrete and other quasibrittle materials. CRC Press; 1998. https://doi.org/10.1201/9780203756799.
[46] Dávila CG, Camanho PP, Rose CA. Failure criteria for FRP laminates. J Compos Mater 2005;39(4):323–45. https://doi.org/10.1177/0021998305046452.
[47] Pinho S.T., Dávila C.G., Camanho P.P., Iannucci L., Robinson P.. Failure models and criteria for FRP under in-plane or three-dimensional stress states including shear non-linearity. 2005. NASA/TM-2005-213530.
[48] C. Chamis C. Simplified composite micromechanical equations for strength, fracture toughness, impact resistance and environmental effects. Tech. rep., Lewis Research Center, Cleveland. 1984.
[49] Carrara P, Ferretti D, Freddi F, Rosati G. Shear tests of carbon fiber plates bonded to concrete with control of snap-back. Eng Fract Mech 2011;78(15):2663–78. https://doi.org/10.1016/j.engfracmech.2011.07.003.
[50] Maimí P, Camanho P, Mayugo J, Dávila C. A continuum damage model for composite laminates: part II - computational implementation and validation. Mech Mater 2007;39(10):909–19. https://doi.org/10.1016/j.mechmat.2007.03.006.
[51] Gama BA, Gillespie JW. Finite element modeling of impact, damage evolution and penetration of thick-section composites. Int J Impact Eng 2011;38(4):181–97. https://doi.org/10.1016/j.ijimpeng.2010.11.001.
[52] Ridruejo A, González C, LLorca J. Micromechanisms of deformation and fracture of polypropylene nonwoven fabrics. Int J Solids Struct 2011;48(1):153–62. https://doi.org/10.1016/j.ijsolstr.2010.09.013.
[53] Raimondo L, Iannucci L, Robinson P, Curtis P. A progressive failure model for mesh-size-independent fe analysis of composite laminates subject to low-velocity impact damage. Compos Sci Technol 2012;72(5):624–32. https://doi.org/10.1016/j.compscitech.2012.01.007.
[54] Bouvet C, Rivallant S, Barrau J. Low velocity impact modeling in composite laminates capturing permanent indentation. Compos Sci Technol 2012;72(16):1977–88. https://doi.org/10.1016/j.compscitech.2012.08.019.
[55] Wu Z, Zhang L, Ying Z, Ke J, Hu X. Low-velocity impact performance of hybrid 3d carbon/glass woven orthogonal composite: experiment and simulation. Comp Part B 2020;196:108098. https://doi.org/10.1016/j.compositesb.2020.108098.